

CONFIDENTIAL

Copy
RM L51K06

APR 18 1952

NACA

RESEARCH MEMORANDUM

LONGITUDINAL STABILITY AND DRAG CHARACTERISTICS AT MACH
NUMBERS FROM 0.75 TO 1.5 OF AN AIRPLANE CONFIGURATION
HAVING A 60° SWEPT WING OF ASPECT RATIO 2.24 AS
OBTAINED FROM ROCKET-PROPELLED MODELS

By A. James Vitale, John C. McFall, Jr.,
and John D. Morrow

Langley Aeronautical Laboratory
Langley Field, Va.

UNCLASSIFIED

FOR REFERENCE

To: _____

By authority of *NACA Res also effective*
ARN-122 Date *Nov. 8, 1957*

NOT TO BE TAKEN FROM THIS ROOM

AMT 12-19-57

CLASSIFIED DOCUMENT

This material contains information affecting the National Defense of the United States within the meaning of the espionage laws, Title 18, U.S.C., Secs. 793 and 794, the transmission or revelation of which in any manner to unauthorized person is prohibited by law.

NATIONAL ADVISORY COMMITTEE
FOR AERONAUTICS

WASHINGTON

April 11, 1952

CA LIBRARY
LANGLEY AERONAUTICAL LABORATORY
Langley Field, Va.

CONFIDENTIAL

NACA RM L51K06



NATIONAL ADVISORY COMMITTEE FOR AERONAUTICS

RESEARCH MEMORANDUM

LONGITUDINAL STABILITY AND DRAG CHARACTERISTICS AT MACH
NUMBERS FROM 0.75 TO 1.5 OF AN AIRPLANE CONFIGURATIONHAVING A 60° SWEPT WING OF ASPECT RATIO 2.24 AS

OBTAINED FROM ROCKET-PROPELLED MODELS

By A. James Vitale, John C. McFall, Jr.,
and John D. Morrow

SUMMARY

Flight tests at Mach numbers from 0.75 to 1.50 have been made of a rocket-propelled airplane configuration model and of a drag model, each having a 60° swept wing of aspect ratio 2.24 with different fuselages. The longitudinal stability, control, and drag characteristics of the airplane configuration were determined by analysis of the response of the model to disturbances in pitch. The minimum-drag characteristics of the drag model were obtained from the zero-lift decelerations of this model.

The lift-curve slope of the airplane configuration model had a very small variation throughout the Mach number range investigated and was affected very little by the elasticity of the wing. A small rearward movement of the aerodynamic center with Mach number was found which appeared to be associated with changes in downwash on the tail. Little variation with Mach number in the percentage of total normal force carried by the exposed wing was noted for the airplane configuration, and the assumptions that the fuselage lift is proportional to the wing area or the portion of span loading diagram intercepted by the fuselage are approximately correct up to a Mach number of 1.56. The zero-lift drag of the wing was a small part of the drag of the complete airplane configuration model and the drag rise was at a Mach number of about 0.90. The drag model had a drag-rise Mach number of 0.975 and low transonic and supersonic drag. The variation of drag with lift coefficient showed that the drag due to lift was smaller by about one-third at supersonic speeds and one-fourth at subsonic speeds than would have been expected if there had been no leading-edge suction.

INTRODUCTION

A general research program utilizing rocket-propelled models in free flight is being conducted by the National Advisory Committee for Aeronautics to determine the transonic and supersonic longitudinal stability, control, and drag characteristics of airplane configurations (references 1 to 3). The method of obtaining this information involves an analysis of the response of the model to disturbances in pitch and is presented in detailed form in reference 1.

The purpose of this paper is to present the results from the flight of a model having a wing with the quarter-chord line swept back 60° , aspect ratio 2.24, and taper ratio 0.33. The airfoil sections of the wing perpendicular to the 32.66-percent-chord line were NACA 64₍₁₀₎A011 at the root and NACA 64A008 at the tip. The wing was similar to the variable-sweep wing of the Bell X-5 research airplane in the 60° sweptback position without the 53° swept-leading-edge fillet. The wing-off longitudinal characteristics of the model are presented in reference 2, the fuselage and tail surfaces being similar to the three models in reference 2.

An all-movable horizontal tail was used for longitudinal control on the airplane configuration, and during the flight the horizontal tail was moved between deflections of 2° to -1° in an approximate square-wave program. An analysis of the flight time history of the response of the model to the horizontal-tail motions was made to determine the longitudinal stability, control, and drag characteristics between Mach numbers from 0.75 to 1.50.

The minimum-drag characteristics of the wing of this configuration were obtained from the flight of a model with a similar wing but different fuselage. The technique for obtaining this information is presented in reference 4.

The models were flown at the Langley Pilotless Aircraft Research Station at Wallops Island, Va.

SYMBOLS

C_N normal-force coefficient $\left(\frac{a_n}{g} \frac{W/S}{q} \right)$

C_c chord-force coefficient $\left(-\frac{a_l}{g} \frac{W/S}{q} \right)$

C_L	lift coefficient $(C_N \cos \alpha - C_c \sin \alpha)$
C_D	drag coefficient $(C_c \cos \alpha + C_N \sin \alpha)$
C_m	pitching-moment coefficient
C_{m_0}	pitching-moment coefficient at zero angle of attack and zero elevator deflection
N_W	wing normal force, pounds
N_A	complete model normal force, pounds
c	wing chord, feet
\bar{c}	wing mean aerodynamic chord, feet
a_n	normal acceleration as obtained from accelerometer, feet per second per second
a_z	longitudinal acceleration as obtained from accelerometer, feet per second per second
g	acceleration due to gravity, feet per second per second
p	free-stream static pressure, pounds per square foot
p_0	standard sea-level static pressure (2116 lb per sq ft)
$b_{e/2}$	exposed wing semispan, feet
$b_{\lambda/2}$	exposed wing semispan measured along 0.40-chord line, feet
y	lateral distance from fuselage side, feet
y_λ	lateral distance from fuselage side measured along 0.40-chord line, feet
G	shear modulus of elasticity, pounds per square inch
L	load applied, pounds
m_θ	wing torsional-stiffness parameter, inch-pounds per radian
m	couple applied near wing tip, inch-pounds
θ	local wing twist angle produced by m , radians; also angle of pitch, radians

α	angle of attack, degrees
δ	horizontal-tail deflection, degrees
ϵ_0	downwash angle at zero angle of attack, degrees
M	Mach number
S	wing area (including the area inclosed within the fuselage), square feet
A	aspect ratio
P	period of oscillation, seconds
R	Reynolds number, based on \bar{c}
$T_{1/2}$	time to damp to one-half amplitude, seconds

Subscripts:

T trim

$$\dot{\alpha} = \frac{1}{57.3} \frac{d\alpha}{dt} \frac{\bar{c}}{2V}$$

$$q = \frac{d\theta}{dt} \frac{\bar{c}}{2V}$$

W wing

A complete model

t tip

b body

MODELS AND APPARATUS

Airplane Configuration

The physical characteristics of the airplane configuration model used in the investigation are shown in figure 1(a), and photographs of the model are given in figure 2. The fuselage and tail surfaces of the

model were similar to those of the airplane configurations presented in reference 2. For the model reported herein the cylindrical portion of the fuselage was lengthened 2 inches forward of the wing section resulting in a body fineness ratio of 13.0. The nose and tail sections of the fuselage are defined by the ordinates in table I. The body frontal area was 10.35 percent of the total wing area.

The wing and horizontal tail were constructed of solid aluminum. The airfoil sections of the wing perpendicular to the 32.66-percent-chord line of the airfoils were NACA 64₍₁₀₎A011 at the root and NACA 64A008 at the tip as shown in the wing layout in figure 1(b). The wing was similar to the Bell X-5 research airplane wing in the 60° swept-back position. The 53° swept-leading-edge fillets were not included in the construction of the wing for the model in the present investigation.

The horizontal tail was mounted on a ball bearing built into the vertical tail and rotated about a hinge line located at 42 percent of the tail mean aerodynamic chord. A hydraulic control system deflected the horizontal tail in an approximate square-wave program. A gap existed between the vertical tail and the root of the horizontal tail. The gap extended over the forward and rearward 30 percent of the horizontal tail root chord and was approximately 0.5 percent of the root chord in width. Similar gaps existed in the three models discussed in reference 2.

The model weighed 124 pounds and the moment of inertia about the pitch axis was 11.49 slug-feet². The center of gravity of the model was at -4.0 percent of the mean aerodynamic chord.

Drag Model

The general arrangement of the drag model is shown in figure 1(c) and photographs of the drag model are given in figure 3. The body had a fineness ratio of 10 with maximum diameter at 40 percent of the body length. Its profile was formed by two parabolic arcs, each having its vertex at the maximum diameter. The body frontal area was 6.06 percent of the total wing area. Body coordinates are found in table II. The wing was identical in plan form and section to the wing flown on the airplane configuration. The quarter-chord point of the wing mean aerodynamic chord was located at 60 percent of the body length. This placed the exposed wing panels behind the body maximum diameter.

With the exception of the magnesium tail fins and body tail cone, the model was of mahogany construction with a polished lacquer finish.

Instrumentation

The airplane configuration model contained a telemeter transmitting measurements of normal acceleration, angle of attack, longitudinal acceleration, wing normal force, control position, total pressure, and a reference static pressure. A vane-type instrument mounted on a sting extending from the nose of the model (fig. 2) was used to measure angle of attack. The angle-of-attack indicator is described in more detail in reference 5.

Wing normal force was measured by mounting the butt of the wing on a beam-type balance (see fig. 4). The balance was designed to permit vertical translation of the wing butt without angular motion. The balance, with a wing mounted on it, is shown in figure 4(a). The vertical motion of the wing relative to the bulkhead was measured by an inductance gage calibrated to give measurements of wing normal force. The balance mounted in the wing section of a model is shown in figure 4(b). The final assembly of the wing section with the hatch and wing in place is shown in figure 4(c). The gaps between the wing butt and the fuselage were sealed inside the fuselage with rubber tubing.

The total-pressure pickup was mounted on a small strut below the fuselage. The static-pressure orifice was located 4.9 inches behind the beginning of the cylindrical portion of the fuselage. A calibration of the reference static pressure for zero angle of attack was obtained from previous instrumentation models.

The drag model contained a telemeter transmitting measurements of longitudinal acceleration and base pressure.

Doppler radar and tracking radar were used to obtain model velocity, range, and elevation as functions of time.

Atmospheric conditions were determined from radiosondes released shortly after the flights. Fixed and manually operated 16-millimeter motion-picture cameras were used to photograph the launchings and first portions of the flights.

Launching Procedures

The airplane configuration model was launched at approximately 45° from the horizontal by means of a crutch-type launcher shown in figure 5. A 6-inch-diameter solid-fuel ABL Deacon rocket motor was used to boost the model to maximum velocity. The model was separated from the booster at booster burnout by the different drag-weight ratios of the model and booster. The model contained no sustaining rocket motor and experienced decelerating flight after separation from the booster.

The drag model was launched from a mobile launcher at approximately 65° from horizontal. A photograph of the model on the launcher is shown in figure 6. The model was not boosted but contained a 6-inch-diameter ABL Deacon rocket motor as a sustainer.

Preflight Measurements

The measured torsional rigidity characteristics of the airplane configuration wing are shown in figure 7. In figure 7(a) a couple was applied near the tip in the free-stream direction and twist measurements were made along the wing parallel to the free stream. For the data in figure 7(b) the couple was applied perpendicular to the 40-percent-chord line and twist measurements were made along the wing perpendicular to the 40-percent-chord line. A photograph of the wing and the test equipment used is shown in figure 7(c). The torsional-stiffness characteristics of the wing are presented as the nondimensional parameter Gc_t^3/m_θ , which is independent of size and material of construction.

Twist in the free-stream direction per unit load applied at various loading stations along the 25- and 50-percent-chord lines is shown in figure 8. The wing with the test equipment used is shown in figure 8(c).

For use in comparing the aeroelastic properties of the wing in the present investigation with other results the values of free-stream pressure obtained during the flight divided by standard sea-level pressure are presented in figure 9 as a function of Mach number.

TESTS AND ANALYSIS

Tests

During the decelerating portion of the flight the airplane configuration model experienced short-period oscillations in angle of attack, normal acceleration, longitudinal acceleration, and wing normal force following each elevator deflection.

The measured angle of attack was corrected to the angle of attack at the center of gravity of the model by the method of reference 5. The wing-normal-force measurements were corrected for inertia effects to obtain aerodynamic forces.

For the airplane configuration model, Doppler radar obtained velocity information from maximum velocity to a Mach number of 1.2. Below the Mach number of 1.2 the pressure data were used for obtaining model velocity. Tracking radar obtained flight-path data over the entire flight.

Velocity information for the drag model was obtained by Doppler radar over a Mach number range of 0.6 to 1.5. Tracking radar obtained flight-path data over the entire flight.

Reynolds numbers (based on wing mean aerodynamic chord for each model) obtained during the flights are shown in figure 10.

Analysis

The short-period oscillations following each horizontal-tail deflection were analyzed by the methods of appendix A, reference 1, to determine the longitudinal stability, control, and drag characteristics of the airplane configuration model.

Below a Mach number of 0.95 the data for the 2.0° horizontal-tail deflection were not used. These oscillations were irregular in nature and could not be analyzed by the method of appendix A, reference 1. The same type of oscillations were observed in unpublished data and the probable cause for the irregular oscillations is thought to be effects of yaw.

The wing-minimum-drag characteristics were obtained from the drag model by the technique of reference 4.

ACCURACY

Airplane Configuration Model

The absolute accuracy of the instruments cannot be stated precisely because the instrument calibrations cannot be checked during or after the flight. Most of the probable instrument errors occur as errors in absolute magnitude and, in general, should be proportional to a certain percentage of the total calibrated range of the instrument. The following table gives estimated values of the possible systematic errors in the absolute values of C_L and C_D , as affected by instrument calibration ranges:

M	ΔC_L	ΔC_D
1.5	± 0.007	± 0.001
1.1	$\pm .016$	$\pm .0025$
.8	$\pm .033$	$\pm .0050$

Further errors in the aerodynamic coefficients may arise because of possible dynamic-pressure inaccuracies which are approximately twice as great as the errors in Mach number. Doppler radar information was obtained for this model from peak velocity to a Mach number of 1.2. Flight-path data were obtained by tracking radar over the entire flight of the model. A consideration of all the factors involved indicates that the Mach numbers are accurate to ± 1 percent at supersonic speeds and ± 2 percent at subsonic speeds.

The errors in the measured angles of attack and horizontal-tail deflections should not vary with Mach number because they are not dependent on dynamic pressure. The horizontal-tail deflections should be accurate to $\pm 0.1^\circ$ and the increments in angle of attack to about $\pm 0.2^\circ$. An error in the absolute magnitude of the angle of attack measurements could be caused by asymmetry of the angle-of-attack vane which is not detectable prior to flight.

The wing normal-force measurements were corrected for the inertia effects of the wing and moving parts of the wing balance. Since this correction is directly proportional to the normal acceleration, the accuracy of the corrected values of wing normal force depends upon the accuracy of two instruments. Due to possible instrumentation errors, the absolute magnitude of wing normal force may be in error by ± 45 pounds. The slope of the curve of wing normal force plotted against total airplane normal force is more accurate than the absolute magnitude of either quantity.

Drag Model

The errors in the drag test are estimated to be within the following limits:

Mach number	± 0.005
Drag coefficient based on total wing area	± 0.0005

RESULTS AND DISCUSSION

Lift

Figure 11 shows plots of some typical lift curves obtained during several oscillations. The complete data did not show any nonlinearity of the lift curves from lift coefficients of -0.12 to 0.25 over the Mach number range of 0.95 to 1.56 . The lift data for the 2.0° horizontal-tail deflection could not be used below a Mach number of 0.95 as explained previously.

The lift-curve slope of the complete airplane configuration model had very little variation throughout the Mach number range as shown in figure 12.

The values of $\Delta C_L / \Delta \delta$ shown in figure 13 are in good agreement with the results shown in reference 2 for three similar models.

Figure 14 shows typical plots of wing normal force against the total normal force of the model. The wing normal-force measurements shown were obtained from the wing balance shown in figure 4. The data points were reduced from the telemeter record at 0.02 second intervals and were corrected for inertia effects. The corrected values of wing normal force were plotted against total normal force for the first $1\frac{1}{2}$ to 2 cycles of an oscillation following each horizontal-tail deflection. There was very little scatter in the data points for these plots and no difference was indicated for increasing or decreasing angle of attack.

The slopes of the wing load curves dC_{N_W} / dC_{N_A} are shown in figure 15. It may be seen from figure 15 that the contribution of the wing to the total airplane normal force is approximately constant over the Mach number range covered. Similar results are shown for high subsonic speed measurements in reference 6.

The lift-curve slopes of the model components are shown in figure 16. The exposed-wing values were found by multiplying the lift-curve slope of the complete configuration by the slope dC_{N_W} / dC_{N_A} . The tail component was found from the values of $\Delta C_L / \Delta \delta$ of figure 13 and downwash data obtained from reference 7 below a Mach number of 1.10 and calculated downwash to a Mach number of 1.55. The values for the wing plus fuselage were found by subtracting the tail component from the lift-curve slope of the complete configuration. The lift-curve slopes of the exposed wing and tail (including downwash) were subtracted from the total to find the lift-curve slopes of the fuselage in the presence of the wing.

One of the methods used in calculating component-loads in design work has been the assumption that the fuselage carried that part of the load represented by the wing area intercepted by the fuselage. Assuming that the wing extended to the center line of the model, the ratio of the wing area outboard of the fuselage to the total wing area is 0.671. Using a span loading for this wing from reference 8, the ratio of the load on the exposed wing to the total load is 0.71. The ratio of the lift-curve slope of the exposed wing to that of the wing plus fuselage obtained from figure 16 varies from 0.60 at subsonic speeds to 0.70 at supersonic speeds. These results show that the usual assumptions made

in obtaining component loads give approximately correct answers for this wing up to a Mach number of 1.56.

Comparisons are made in figure 16 between the wing-plus-fuselage lift-curve slopes obtained from the rocket model and two wind-tunnel tests (references 7 and 9). The wing tested in reference 7 differed from the rocket-model wing in airfoil section and had an aspect ratio of 2 compared to 2.24 for the rocket model. The low-speed data for the $\frac{1}{4}$ -scale Bell X-5 research airplane model tested in reference 9 were corrected for compressibility effects by the method of reference 10.

Also shown in figure 16 is the lift-curve slope of the exposed wing corrected for aeroelastic effects. Using a span loading diagram obtained from reference 8 and the twist due to bending data in figure 8, the experimental lift-curve slope was corrected to the rigid case. This correction was found to be very small for the wing tested.

Drag

The minimum-drag results for the airplane and drag configurations are presented in figure 17. Also shown is the drag coefficient variation for the lacquer-finish wingless body of reference 11. This body was identical to that used on the drag model except for two additional tail fins. The high drag and early drag-rise Mach number of the airplane configuration results from the high-drag body and tail and small size of the wing relative to the body. As a result, the wing drag represents a small percentage of the drag of this configuration.

The results for the drag model, however, show the low drag obtained with the test wing. The configuration has a drag-rise Mach number of 0.975 and low transonic and supersonic drag.

The low drag of this configuration will be more evident if compared with the results of reference 11. The dip in drag coefficient at $M = 0.98$ has occurred on similar configurations and probably results from fluctuations in afterbody pressure as is shown in reference 12. The abrupt change in drag coefficient at $M = 1.29$ results from a change in base drag.

Wing-plus-interference drag coefficient obtained from the drag model is shown in figure 18. This was obtained by subtracting the drag of the wingless configuration from the drag of the winged drag model. Due to the fact that the winged model had two fins and the wingless model had four fins, a correction was made for the difference in fin drag based on drag tests of these fins.

In addition, the results were corrected for the difference in base drag between the winged and wingless models. The low-transonic and supersonic drag for this wing indicate what can be obtained with the proper combination of wing sweepback and thickness.

The drag due to lift of the airplane configuration is presented in figure 19. Also shown is the drag due to lift for no leading-edge suction $1/57.3C_{L\alpha}$ and the ideal induced drag factor $1/\pi A$. Since 32.9 percent of the wing area is enclosed within the fuselage, it would be impossible to realize the value $1/\pi A$ for dC_D/dC_L^2 . The results show that leading-edge suction reduced the drag due to lift by approximately 30 percent at supersonic speeds and 25 percent at subsonic speeds.

Values of maximum lift-drag ratio and C_L at which maximum lift-drag ratio occurs are shown in figures 20 and 21 for both the airplane and drag configurations. For the airplane configuration the values were obtained by an extrapolation of the drag polars using the measured values of $C_{D_{min}}$ and dC_D/dC_L^2 . The amount of extrapolation is shown by the curve of maximum lift coefficient reached during the test. It has been assumed that the drag model had the same dC_D/dC_L^2 as the airplane configuration. The high values of $(L/D)_{max}$ and low values of C_L for $(L/D)_{max}$ for the drag model are a reflection of the lower-drag tail, the higher ratio of S_w/S_b , and the low drag of the fuselage of the drag model as compared with the airplane configuration.

Static Stability

The measured periods of oscillation of the angle of attack are shown in figure 22(a). The data converted to the static stability derivative $C_{m\alpha}$ are shown in figure 22(b). Below a Mach number of 1.02 the data are shown for the -1.0° horizontal-tail setting only. Above this Mach number the data do not show any nonlinearity in $C_{m\alpha}$ over the lift range covered.

From the data for the wingless model in reference 2 it should be possible to determine the total effect of the wing on the stability of the airplane. Due to the nonlinearity of $C_{m\alpha}$ and $C_{L\alpha}$ of the wingless model in reference 2, no attempt was made to convert the data to the center-of-gravity position of the model discussed in this paper.

A more complete picture of the static stability is shown in figure 22(c) where the data were converted to aerodynamic-center location of the complete model and the wing-fuselage combination. By multiplying

the lift-curve slope of the tail (including downwash) by the tail length, l_t/\bar{c} , and dividing by Cl_{α} of the complete configuration, the rearward increment in aerodynamic-center location caused by the tail was obtained. The aerodynamic-center position of the wing plus fuselage was obtained by subtracting the tail increment from the aerodynamic center of the complete configuration. The results show that the rearward movement of the aerodynamic center of the complete configuration as the Mach number increases is probably caused by the change in downwash on the tail.

The wing-plus-fuselage aerodynamic center from the rocket-model data is compared with results from two wind-tunnel investigations, references 7 and 9, in figure 22(c). The difference in fuselage size between the rocket model and the $\frac{1}{4}$ -scale model of reference 9 may account for the more rearward aerodynamic-center position for the model of reference 9.

Damping in Pitch

The time required for the pitch oscillations to damp to one-half amplitude is shown in figure 23(a) and the data converted to the damping factor $C_{m_q} + C_{m_{\dot{\alpha}}}$ are shown in figure 23(b). Also shown in figure 23(b) is the damping factor obtained from the wing-off model of reference 2 converted to the center-of-gravity position and dimensions of this model. In the Mach number range shown the pitch damping factor for the wing-off model does not vary much with Mach number.

Since the damping factor $C_{m_q} + C_{m_{\dot{\alpha}}}$ for the wing-off model is essentially the C_{m_q} of the tail, the difference between the complete model and wing-off curves of figure 23(b) is mostly due to the negative $C_{m_{\dot{\alpha}}}$ contributed by the wing and downwash. The sudden change in damping at $M = 0.85$ was also found for a similar model having a triangular wing (from unpublished data), and the reason for this is, as yet, unknown.

Longitudinal Trim and Control Effectiveness

The trim angles of attack and lift coefficients are shown in figure 24 for horizontal-tail deflections of -1.0° and 2.0° . The data indicate an abrupt trim change in both angle of attack and lift coefficient for the -1.0° horizontal-tail deflection between $M = 0.90$ and $M = 1.0$. This same trim change may have occurred for the 2.0° horizontal-tail setting; the number of trim points obtained in

this region was not sufficient to establish the correct fairing of the curves. This same type of change was indicated by the wing-off model of reference 2.

The effectiveness of the horizontal tail in producing pitching moment is shown in figure 25 as incremental values $\Delta C_m / \Delta \delta$. When converted for center-of-gravity position and chord, the $\Delta C_m / \Delta \delta$ for this model agrees very well with the values presented in reference 2 for the wingless model with an identical tail. This repeatability of data obtained from identical components on different models furnishes a very good check on the over-all accuracy of the data.

The pitching-moment coefficients at zero angle of attack and zero horizontal-tail deflection are shown in figure 26. The variation of C_{m_0} with Mach number is about the same for this model and the three models of reference 2. As pointed out in reference 2, C_{m_0} is primarily due to a downflow over the tail caused by the converging rear portion of the fuselage. A small part of C_{m_0} is caused by the drag of the horizontal and vertical tail surfaces. The values of horizontal-tail deflection required to trim the model at zero angle of attack were corrected for the drag of the horizontal and vertical tails to obtain the downwash angle at zero angle of attack shown in figure 27.

CONCLUSIONS

The flight tests of a rocket-propelled model of an airplane configuration having a 60° swept wing of aspect ratio 2.24 and of a drag model having a similar wing but different fuselage indicated the following results over the Mach number range $M = 0.75$ to $M = 1.50$:

1. The variation of the lift-curve slope with Mach number was very small and gradual for the airplane configuration.
2. The part of the total airplane normal force carried by the exposed wing is approximately constant over the Mach number range $M = 0.75$ to $M = 1.56$.
3. The assumptions that the fuselage lift is proportional to the wing area or the portion of span load intercepted by the fuselage are approximately correct for the airplane configuration up to a Mach number of 1.56.
4. The elasticity of the wing had very little effect on the lift-curve slope of the airplane configuration.

5. The zero-lift drag of the wing is a small part of the drag of the airplane configuration. The drag rise Mach number is about 0.90 for this configuration.

6. The drag model has a drag-rise Mach number of 0.975 and low transonic and supersonic drag. The wing-plus-interference drag never exceeded 0.009 over the Mach number range $M = 0.90$ to $M = 1.50$.

7. The drag due to lift was about 30 percent lower at supersonic speeds and 25 percent lower at subsonic speeds than the values that would be obtained with no leading-edge suction.

8. The increase in static stability with Mach number of the airplane configuration is probably caused by change in downwash on the tail.

9. The contribution of the wing to the damping factor decreased with increasing Mach number.

10. Trim angles and trim lift coefficients have a rise of approximately 25 percent from a Mach number of 0.93 to 0.98.

Langley Aeronautical Laboratory
National Advisory Committee for Aeronautics
Langley Field, Va.

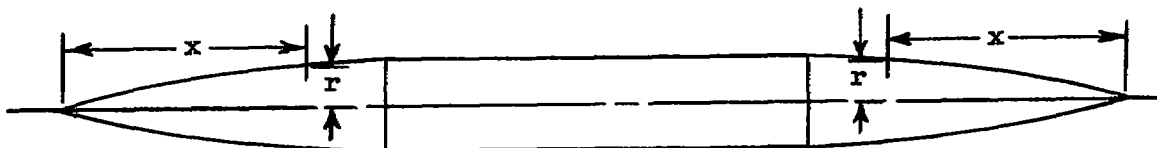
REFERENCES

1. Gillis, Clarence L., Peck, Robert F., and Vitale, A. James: Preliminary Results from a Free-Flight Investigation at Transonic and Supersonic Speeds of the Longitudinal Stability and Control Characteristics of an Airplane Configuration with a Thin Straight Wing of Aspect Ratio 3. NACA RM L9K25a, 1950.
2. Gillis, Clarence L., and Vitale, A. James: Wing-On and Wing-Off Longitudinal Characteristics of an Airplane Configuration Having a Thin Unswept Tapered Wing of Aspect Ratio 3, As Obtained from Rocket-Propelled Models at Mach Numbers from 0.8 to 1.4. NACA RM L50K16, 1951.
3. Mitcham, Grady L., Stevens, Joseph E., and Norris, Harry P.: Aerodynamic Characteristics and Flying Qualities of a Tailless Triangular-Wing Airplane Configuration As Obtained from Flights of Rocket-Propelled Models at Transonic and Low Supersonic Speeds. NACA RM L9L07, 1950.
4. Morrow, John D., and Katz, Ellis: Flight Investigation at Mach Numbers from 0.6 to 1.7 to Determine Drag and Base Pressures on a Blunt-Trailing-Edge Airfoil and Drag of Diamond and Circular-Arc Airfoils at Zero Lift. NACA RM L50E19a, 1950.
5. Mitchell, Jesse L., and Peck, Robert F.: An NACA Vane-Type Angle-of-Attack Indicator for Use at Subsonic and Supersonic Speeds. NACA RM L9F28a, 1949.
6. Mayer, John P., and Valentine, George M.: Flight Measurements with the Douglas D-558-II (BuAero No. 37974) Research Airplane. Measurements of the Distribution of the Aerodynamic Load among the Wing, Fuselage, and Horizontal Tail at Mach Numbers up to 0.87. NACA RM L50J13, 1951.
7. Myers, Boyd C., II, and King, Thomas J., Jr.: Aerodynamic Characteristics of a Wing with Quarter-Chord Line Swept Back 60° , Aspect Ratio 2, Taper Ratio 0.6, and NACA 65A006 Airfoil Section. Transonic-Bump Method. NACA RM L50A12, 1950.
8. De Young, John, and Harper, Charles W.: Theoretical Symmetric Span Loading at Subsonic Speeds for Wings Having Arbitrary Plan Form. NACA Rep. 921, 1948.

9. Kemp, William B., Jr., Becht, Robert E., and Few, Albert G., Jr.:
Stability and Control Characteristics at Low Speed of a $\frac{1}{4}$ -Scale
Bell X-5 Airplane Model. Longitudinal Stability and Control. NACA
RM L9K08, 1950.
10. Fisher, Lewis R.: Approximate Corrections for the Effects of
Compressibility on the Subsonic Stability Derivatives of Swept
Wings. NACA TN 1854, 1949.
11. Schult, Eugene D.: Large-Scale Flight Measurements of Zero-Lift
Drag at Mach Numbers from 0.8 to 1.6 of a Wing-Body Combination
Having an Unswept 4.5-Percent-Thick Wing with Modified Hexagonal
Sections. NACA RM L51A15, 1951.
12. Stoney, William E., Jr.: Pressure Distributions at Mach Numbers
from 0.6 to 1.9 Measured in Free Flight on a Parabolic Body of
Revolution with Sharply Convergent Afterbody. NACA RM L51L03,
1952.

TABLE I

FUSELAGE NOSE AND TAIL ORDINATES FOR
AIRPLANE CONFIGURATION

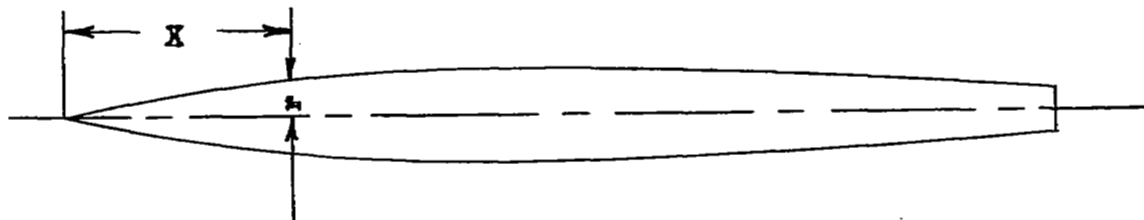


x (in.)	r (in.)
0	0.168
.060	.182
.122	.210
.245	.224
.480	.294
.735	.350
1.225	.462
2.000	.639
2.450	.735
4.800	1.245
7.350	1.721
8.000	1.849
9.800	2.155
12.250	2.505
13.125	2.608
14.375	2.747
14.700	2.785
17.150	3.010
19.600	3.220
22.050	3.385
24.500	3.500



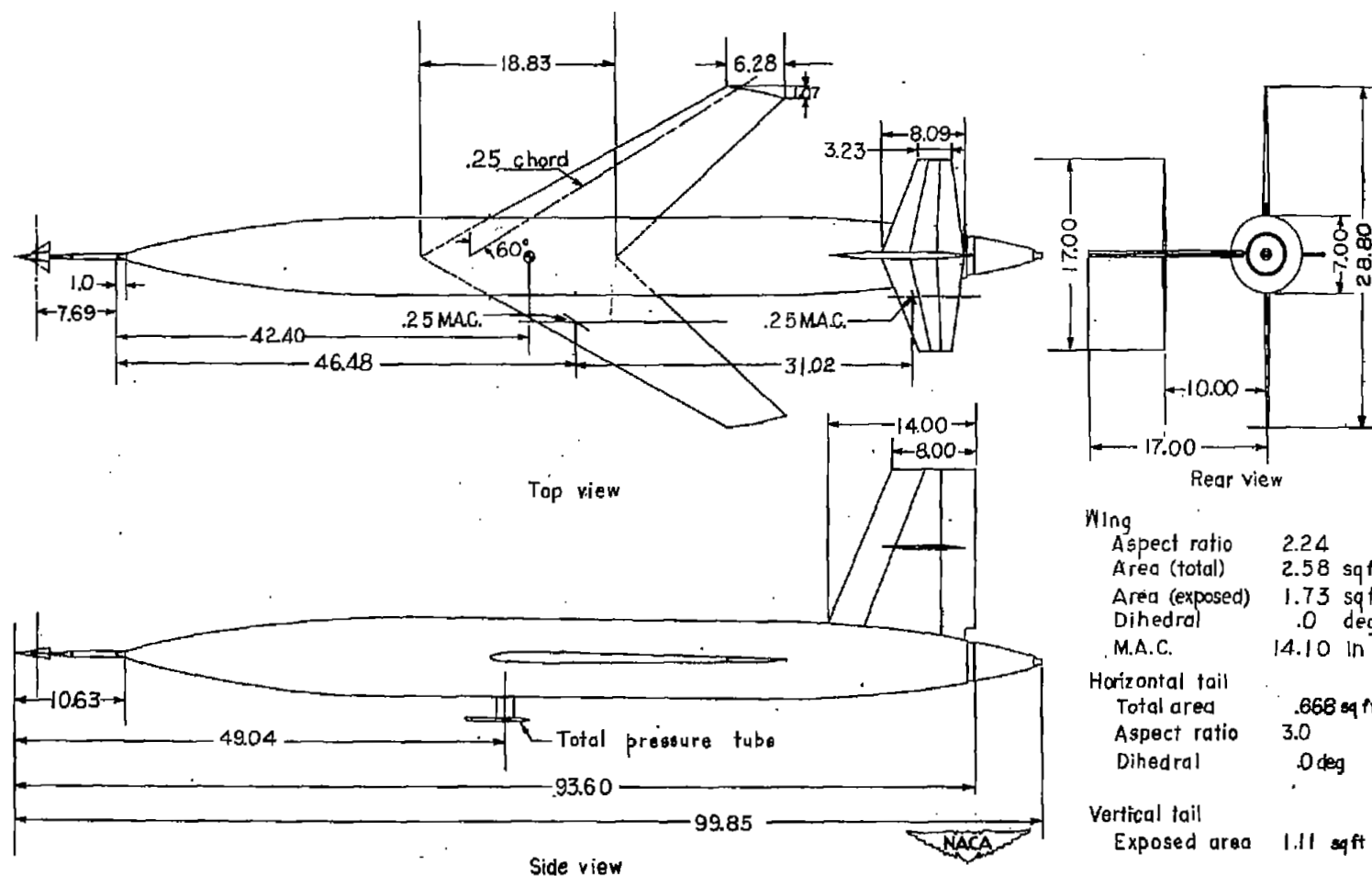
TABLE II

BODY ORDINATES FOR DRAG MODEL



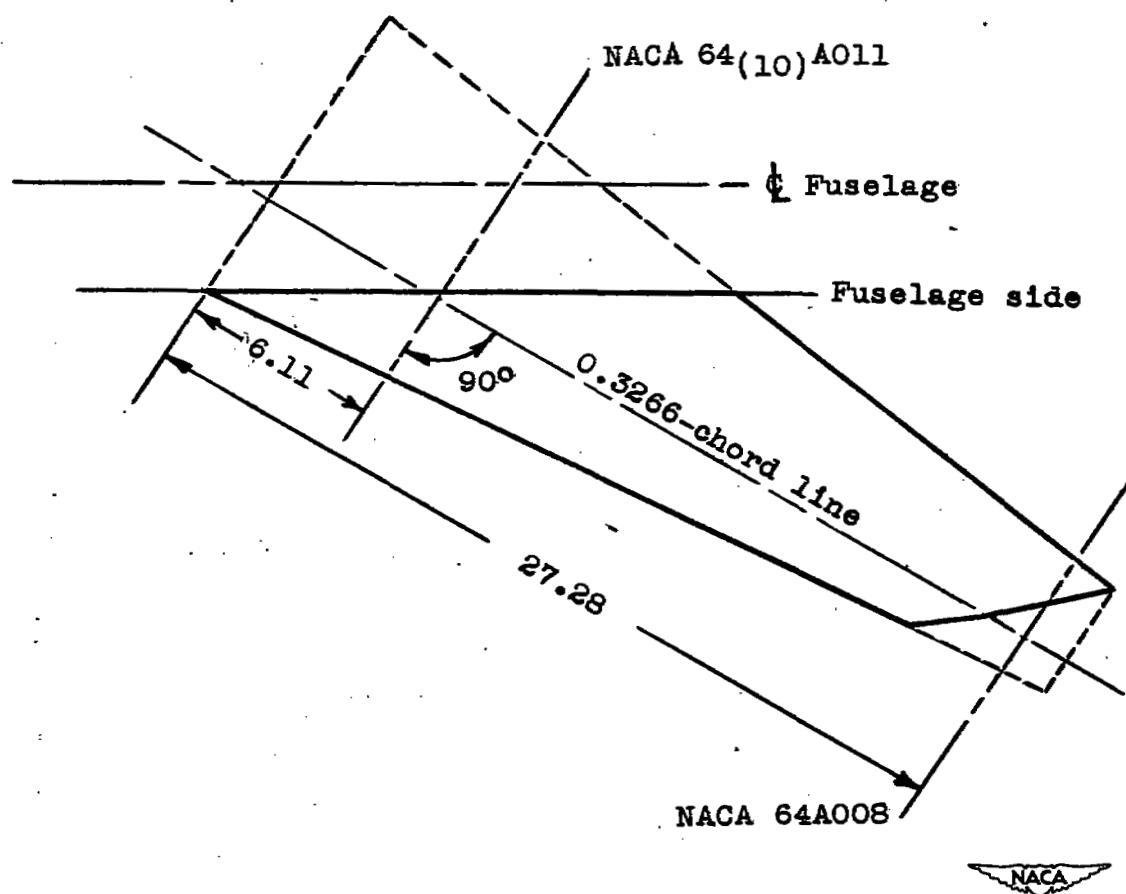
Body coordinates 130-inch parabolic model (in.)			
X	r	X	r
0	0	54.60	6.496
.78	.194	62.40	6.442
1.17	.289	70.20	6.322
1.95	.478	78.00	6.137
3.90	.938	85.80	5.886
7.80	1.804	93.60	5.570
11.70	2.596	101.40	5.188
15.60	3.315	109.20	4.742
23.40	4.534	117.00	4.229
31.20	5.460	124.80	3.652
39.00	6.094	130.00	3.230
46.80	6.435		





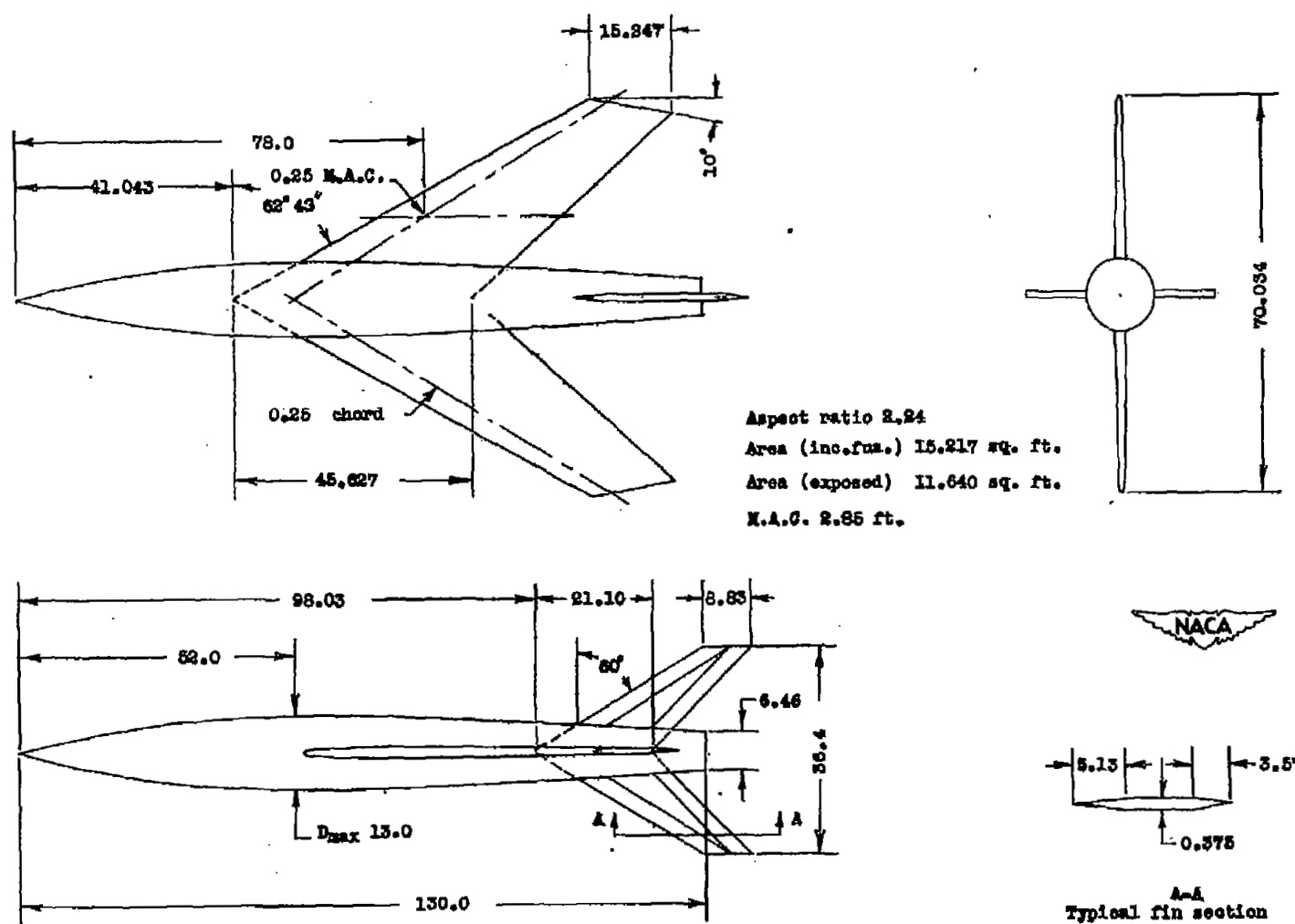
(a) General arrangement of airplane configuration model.

Figure 1.- Physical characteristics of models. All dimensions in inches.



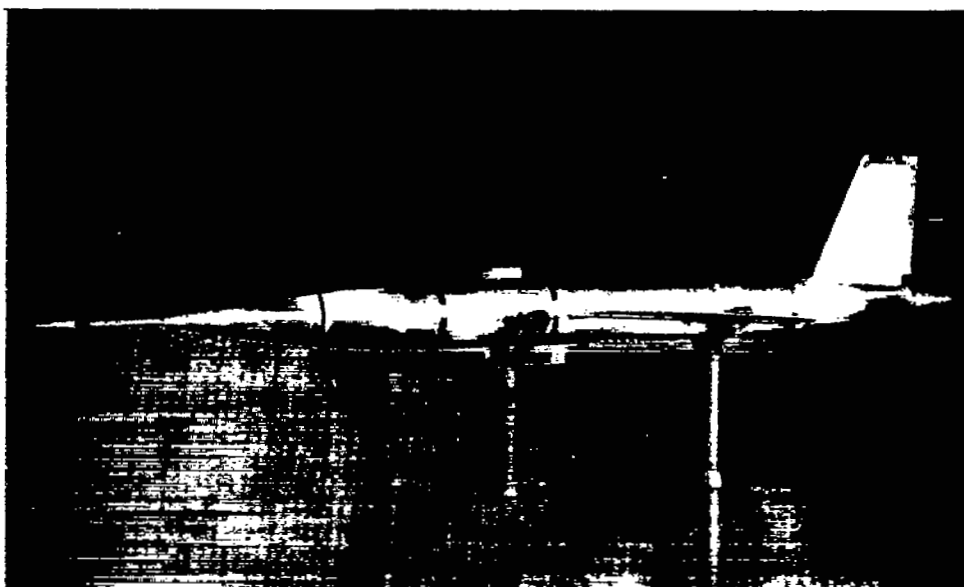
(b) Wing detail of airplane configuration model.

Figure 1.- Continued.



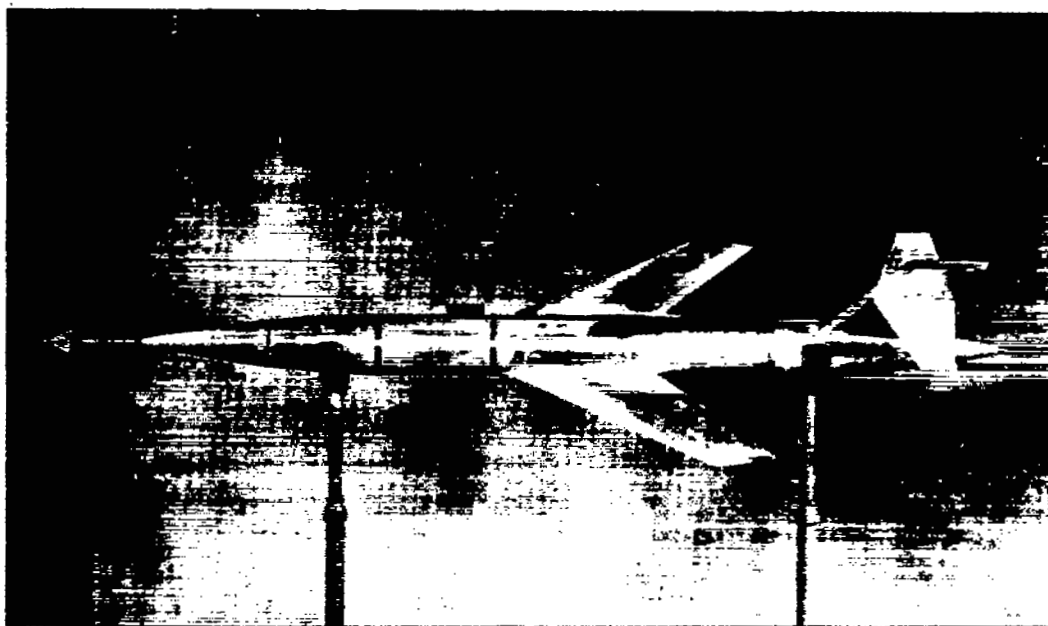
(c) General arrangement of drag model.

Figure 1.- Concluded.



(a) Three-quarter front view.

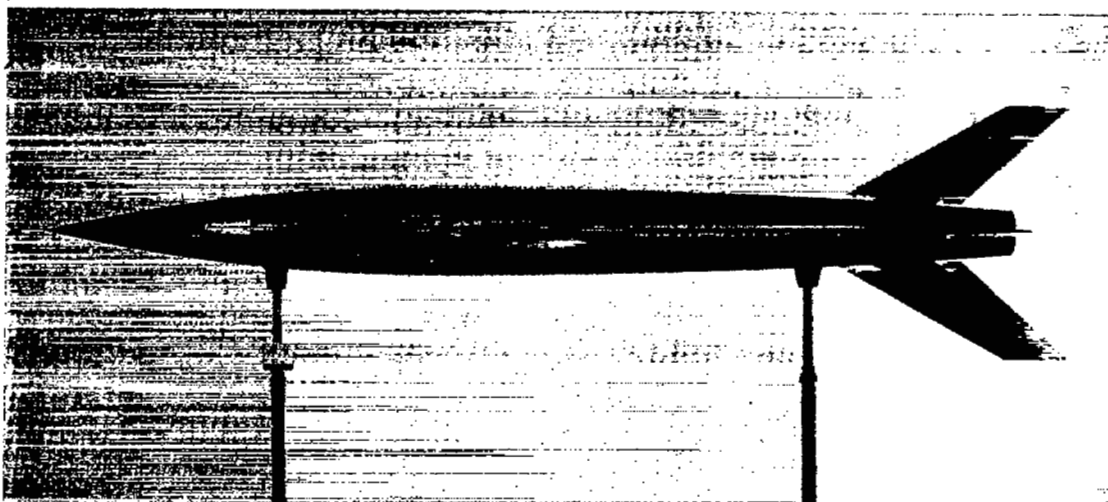
NACA
L-64753



(b) Top view.

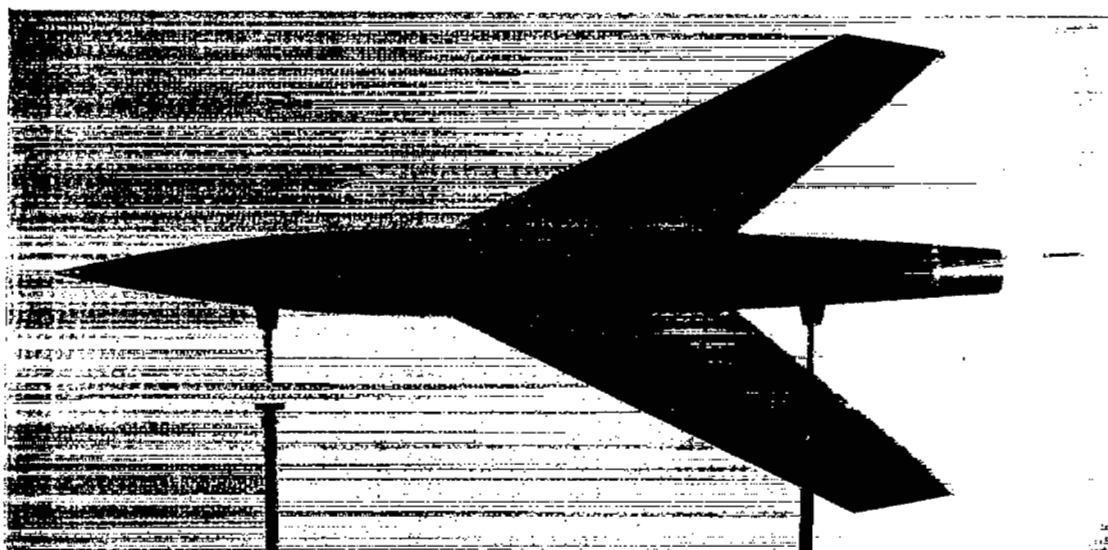
Figure 2.- Photographs of airplane configuration model.

NACA
L-64754



(a) Side view.

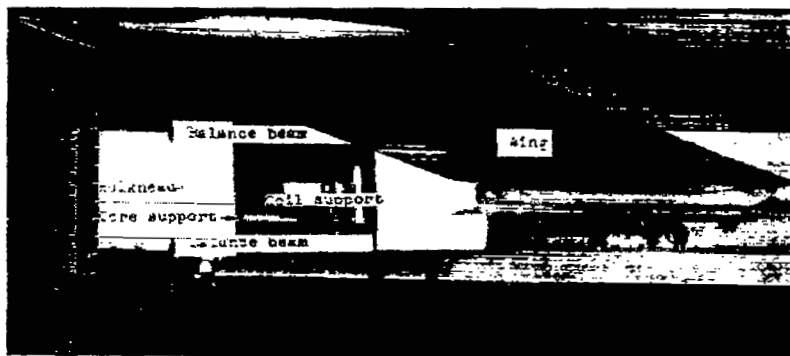
NACA
L-69828



(b) Top view.

Figure 3.- Photographs of drag model.

NACA
L-69829



(a) Wing balance components.

NACA
L-68860.1



(b) Wing section with hatch off.

NACA
L-68566.1



(c) Wing section.

Figure 4.- Wing normal-force balance.

NACA
L-64756



NACA
L-66365

(a) Side view.



(b) Top view.

NACA
L-66366

Figure 5.- Airplane configuration model on launcher.

NACA RM L51K06

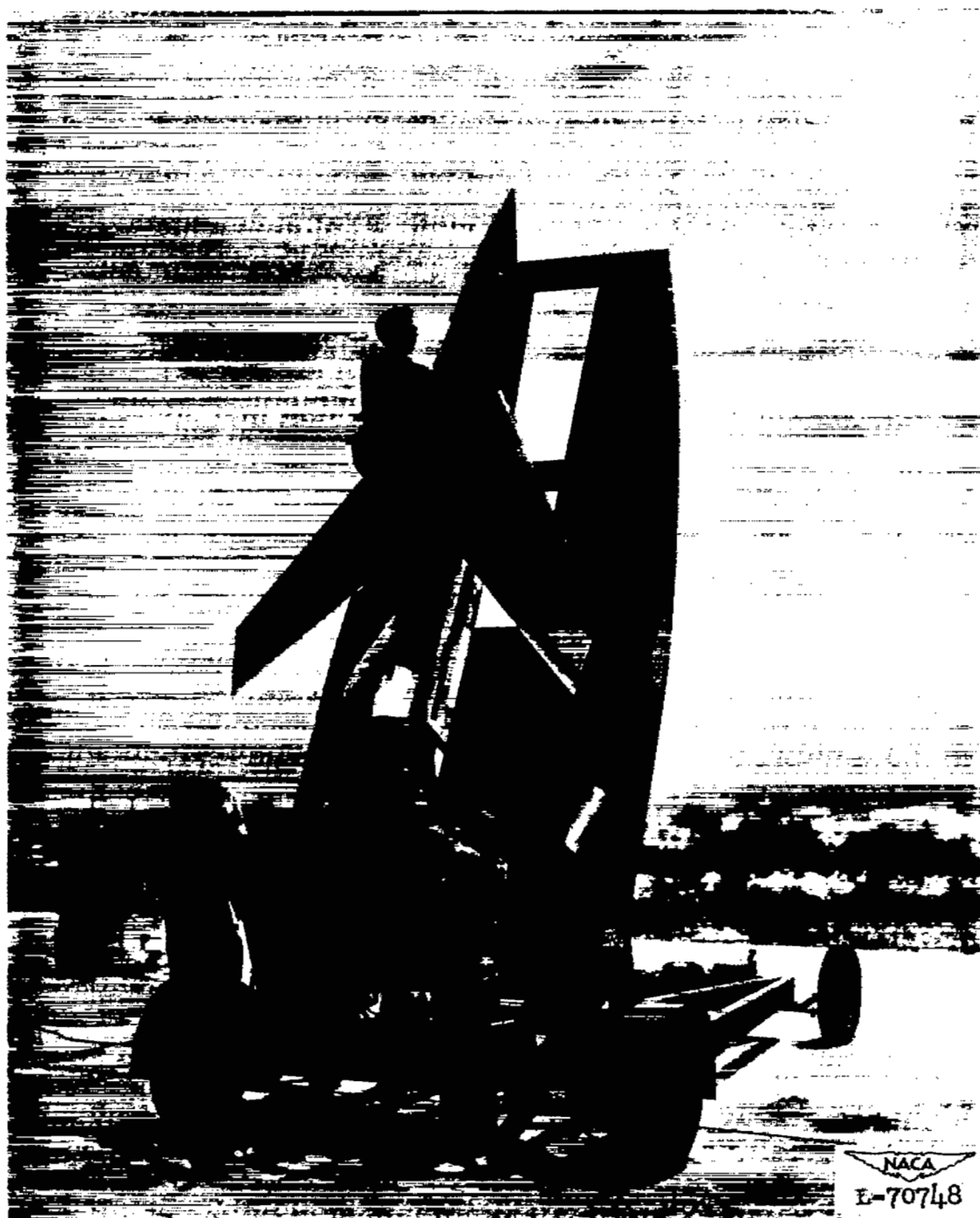
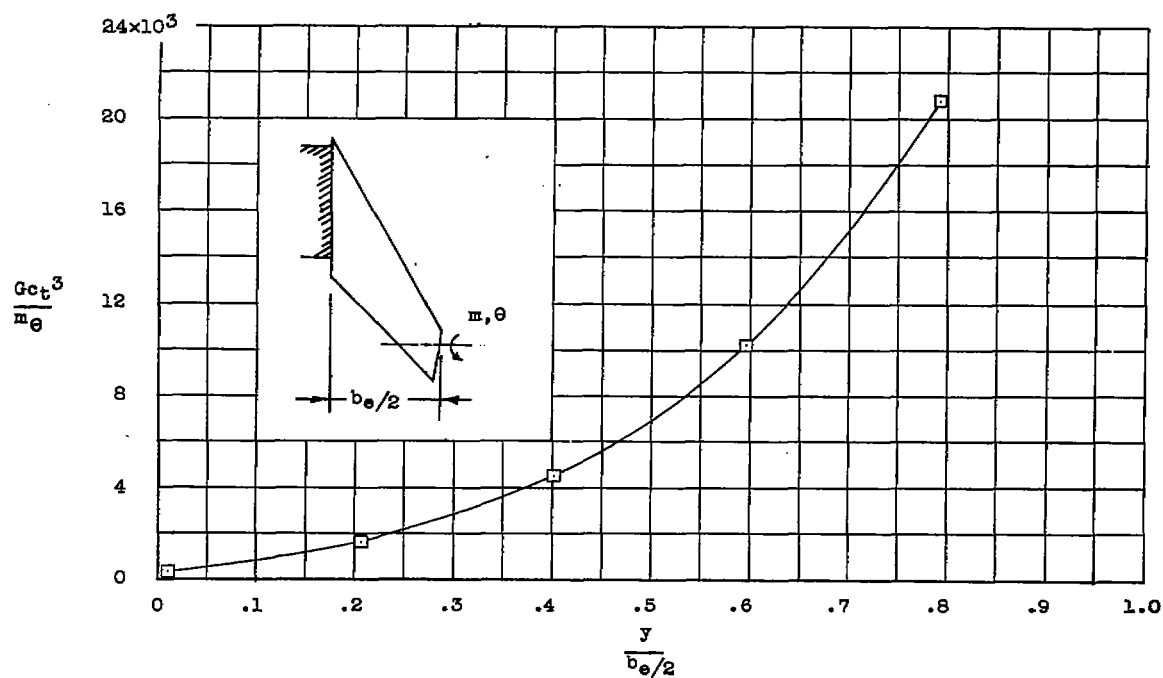
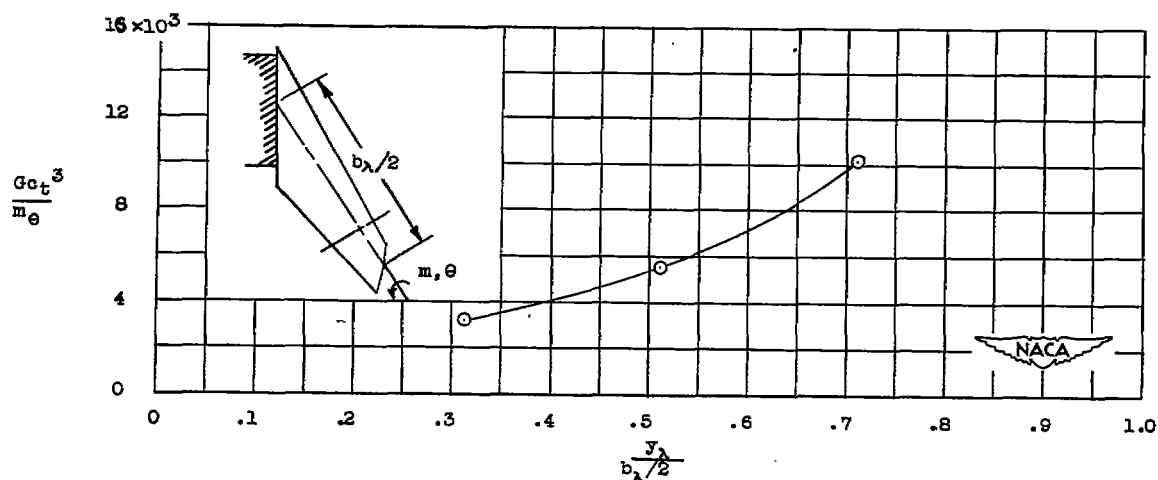


Figure 6.- Drag model on mobile launcher.

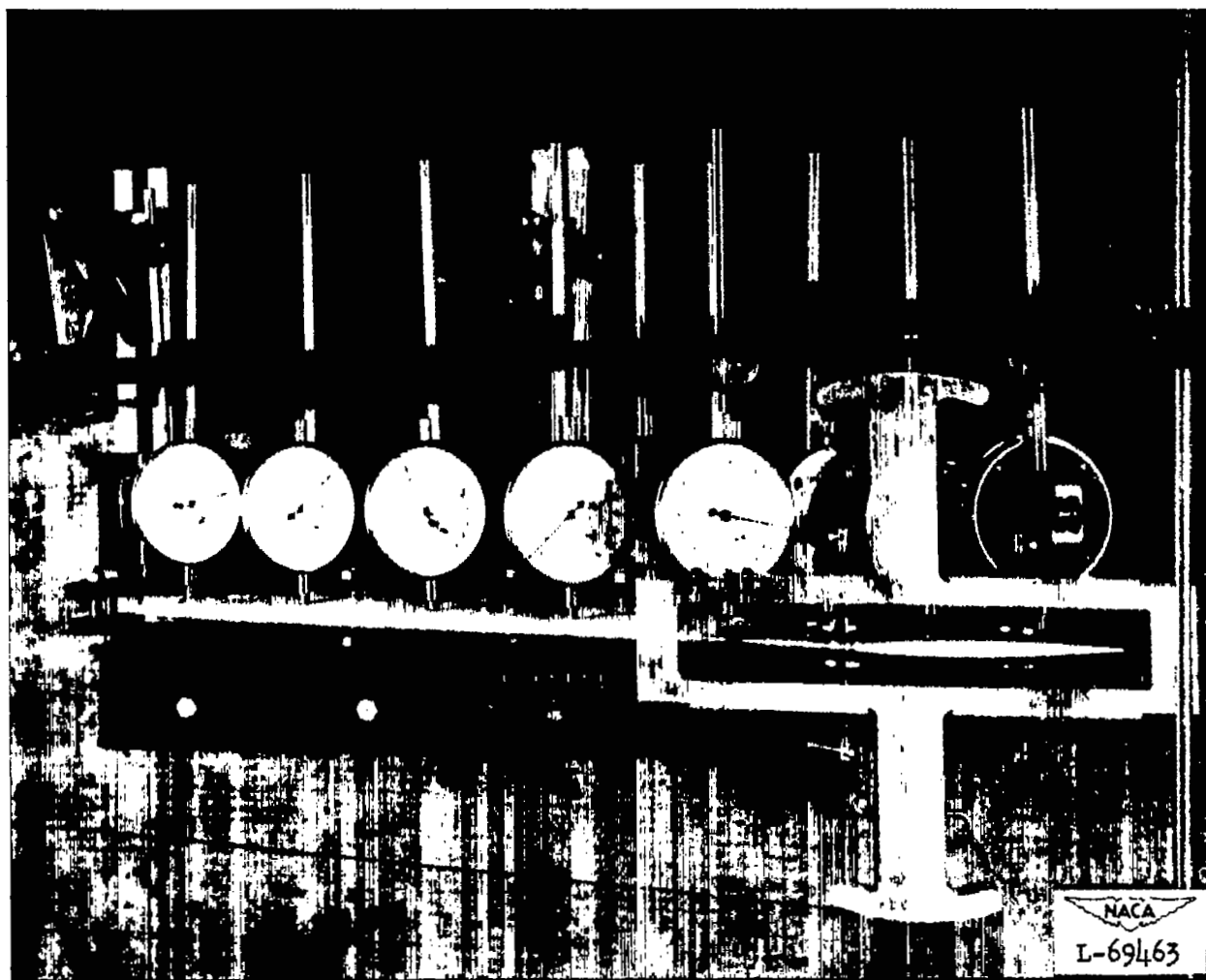


(a) Parallel to free stream.



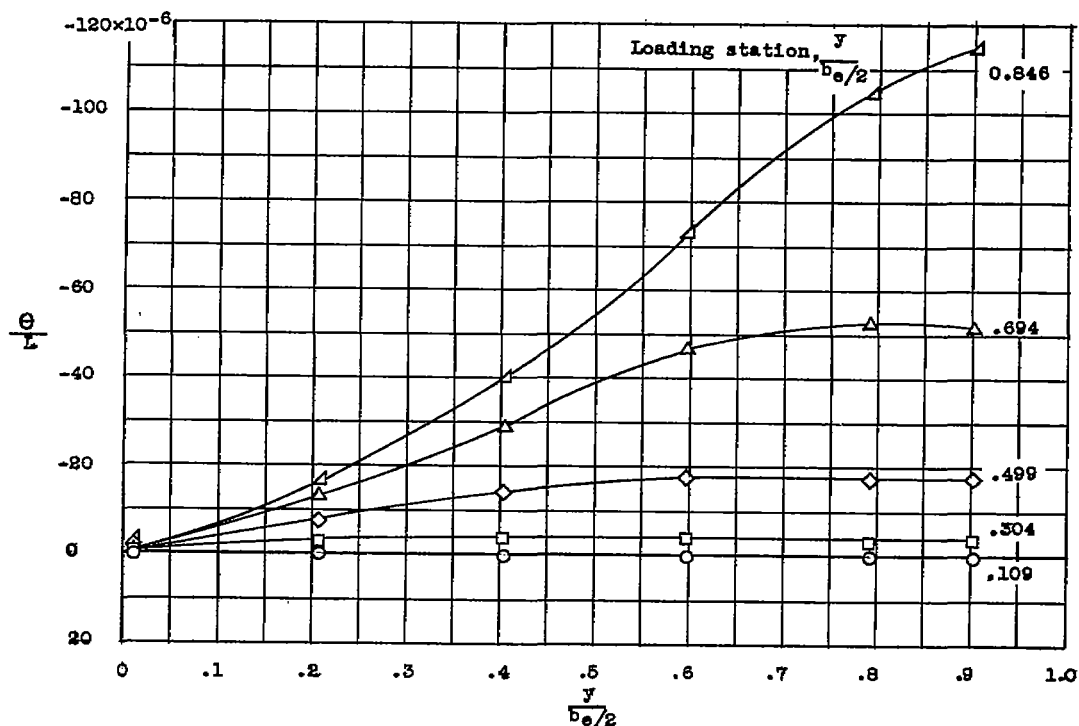
(b) Perpendicular to the 40-percent-chord line.

Figure 7.- Measured torsional rigidity of wing.

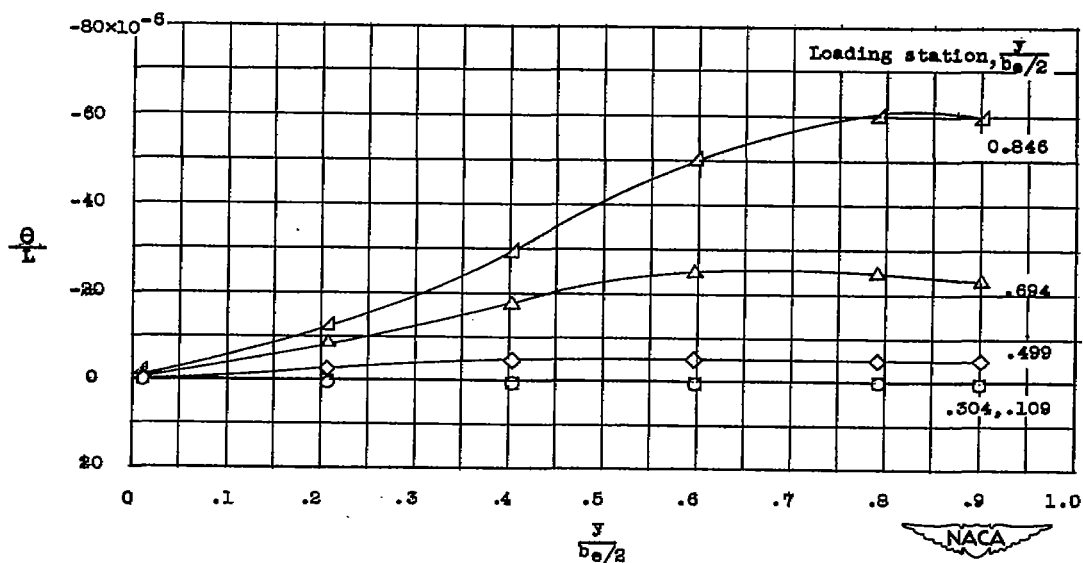


(c) Photograph of test setup for obtaining torsional-rigidity data.

Figure 7.- Concluded.

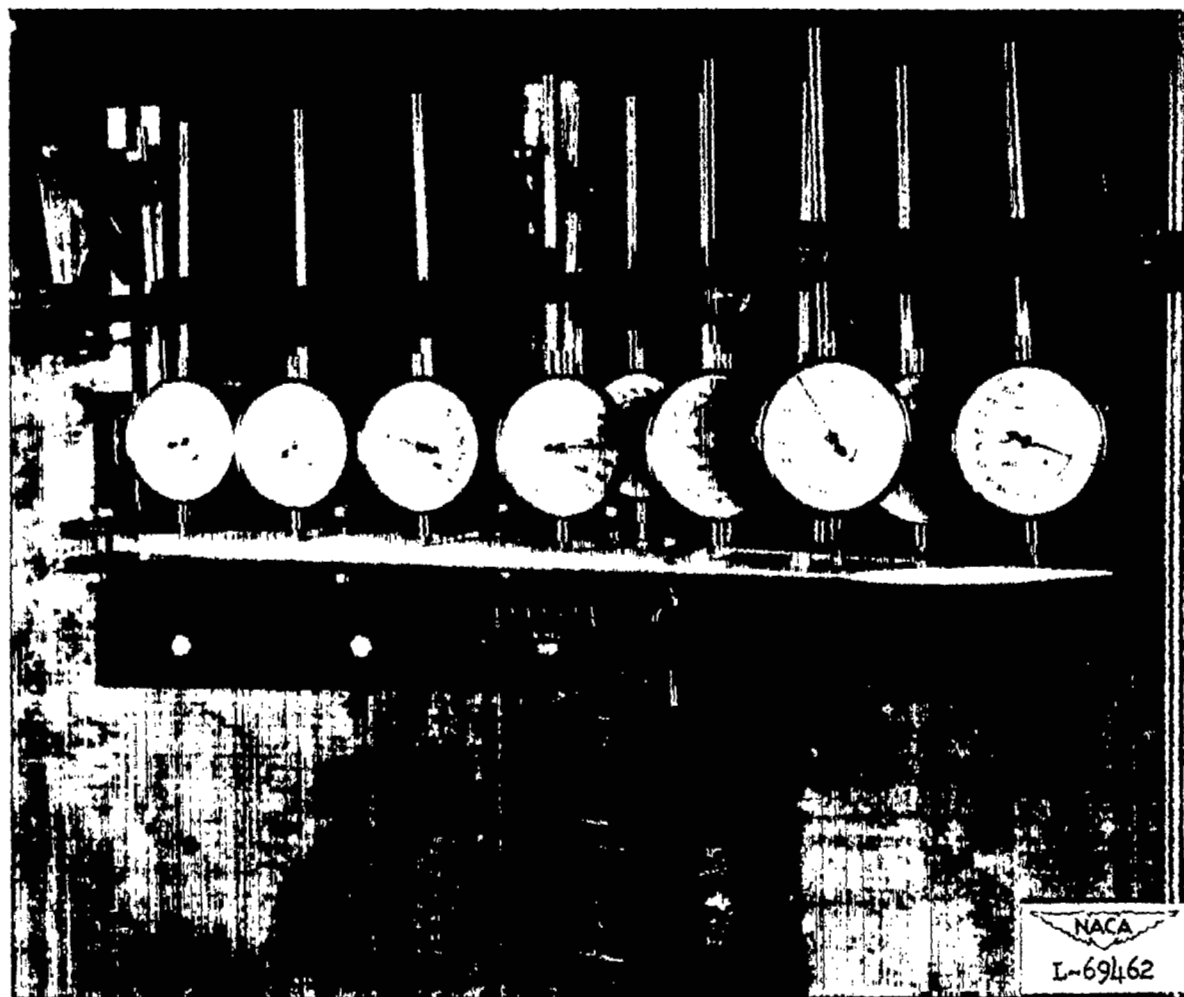


(a) Load applied along the 50-percent-chord line.



(b) Load applied along the 25-percent-chord line.

Figure 8.- Twist in the free-stream direction per unit load applied at various stations along the span.



(c) Photograph of test setup for obtaining twist due to bending.

Figure 8.- Concluded.

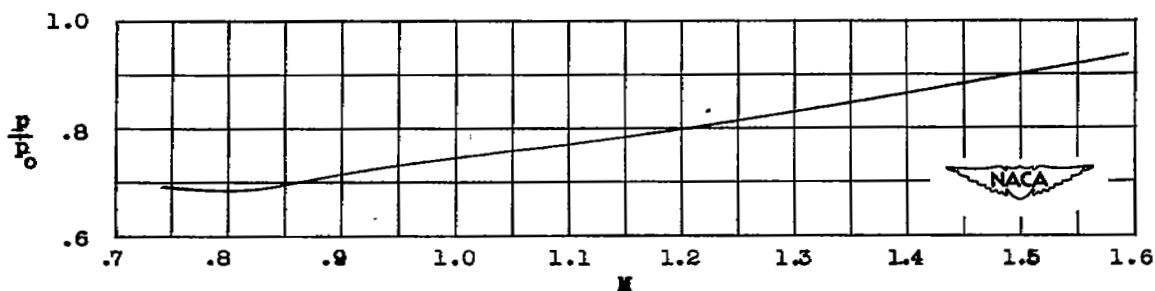


Figure 9.- Static-pressure ratio.

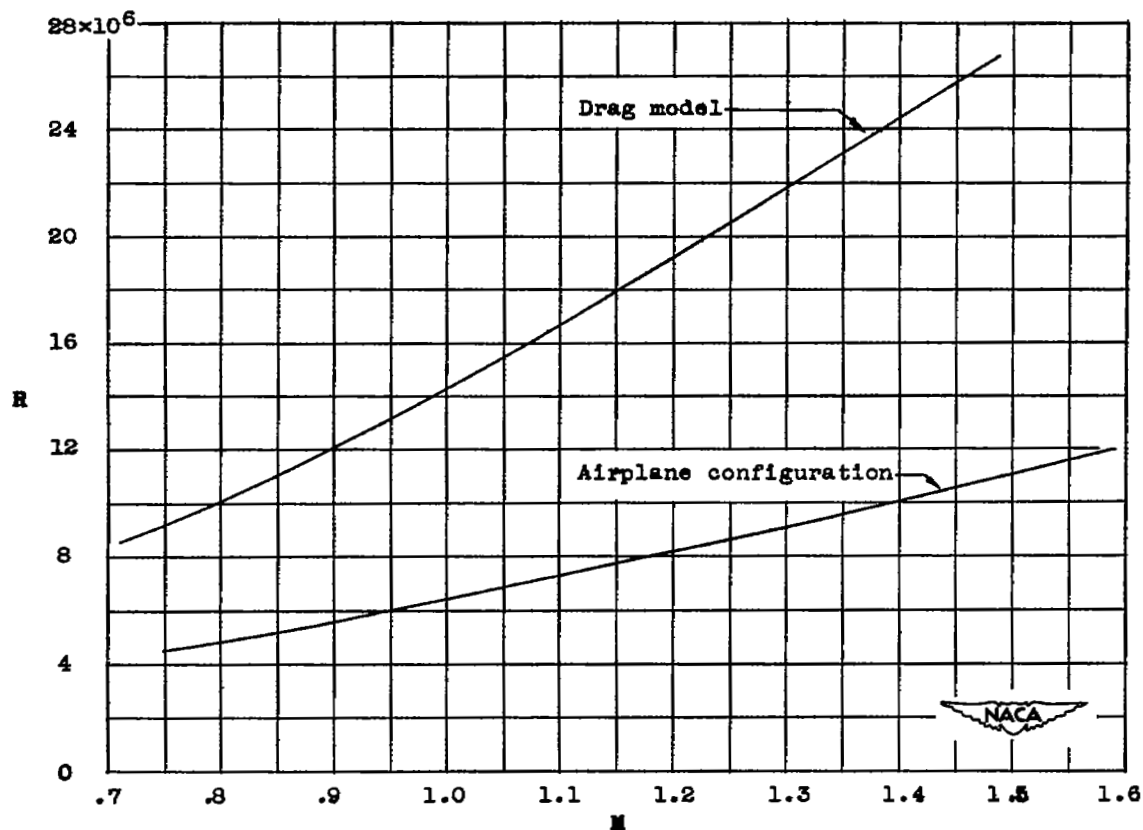


Figure 10.- Reynolds number of tests, based on mean aerodynamic chords.

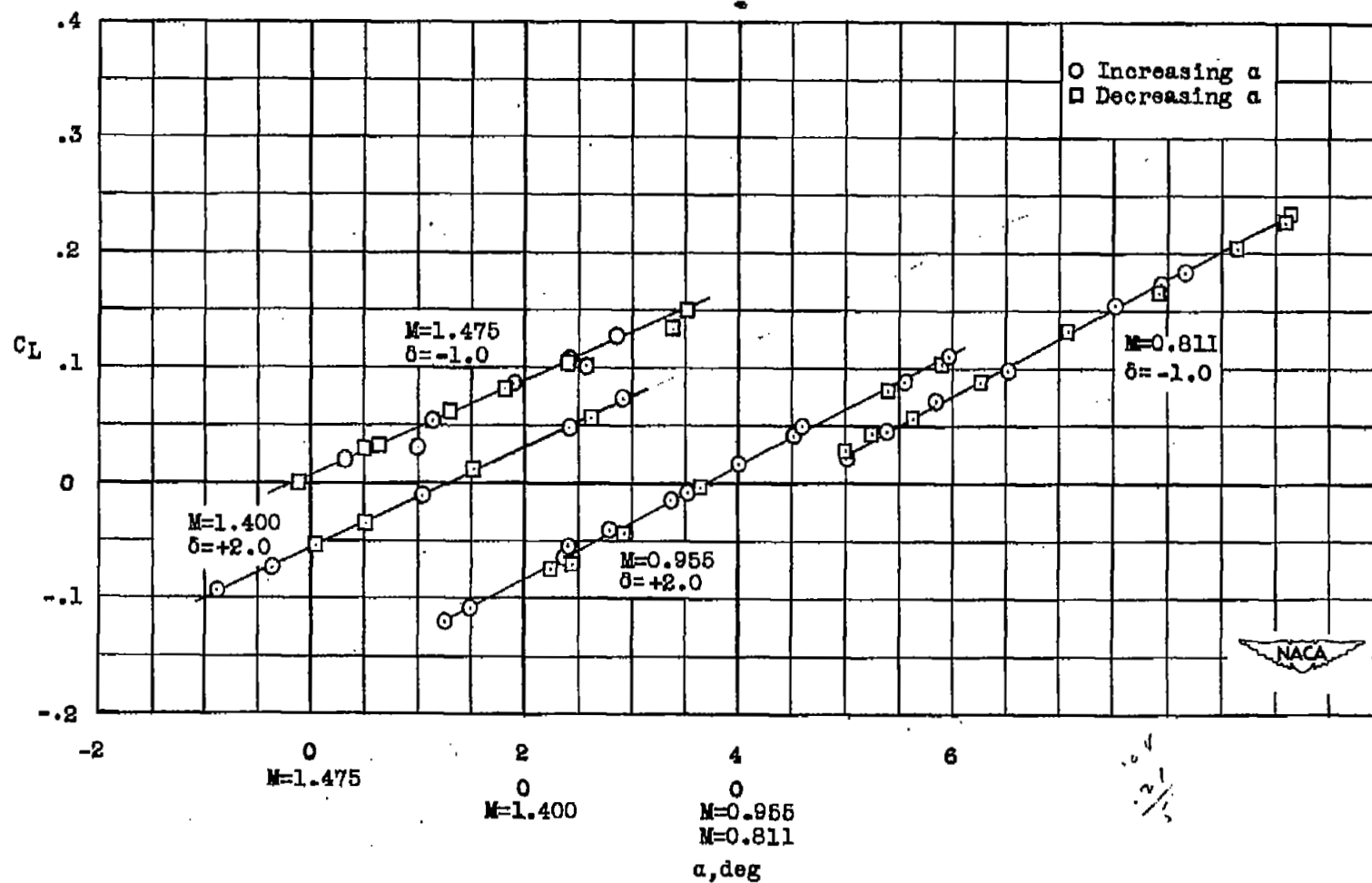


Figure 11.- Typical lift curves.

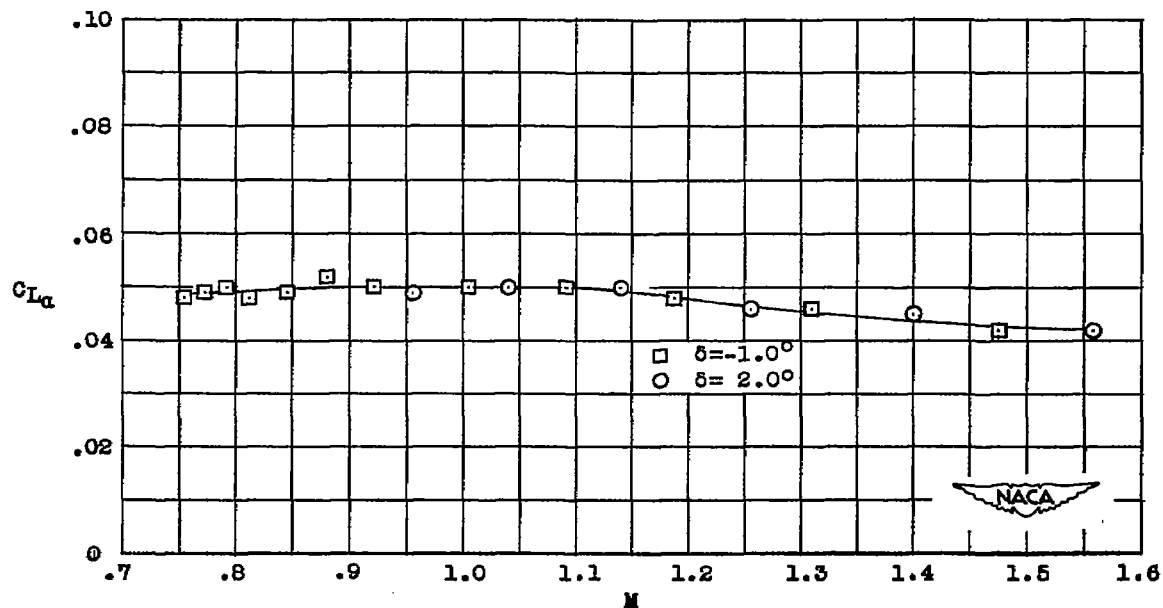


Figure 12.- Lift-curve slope of complete model.

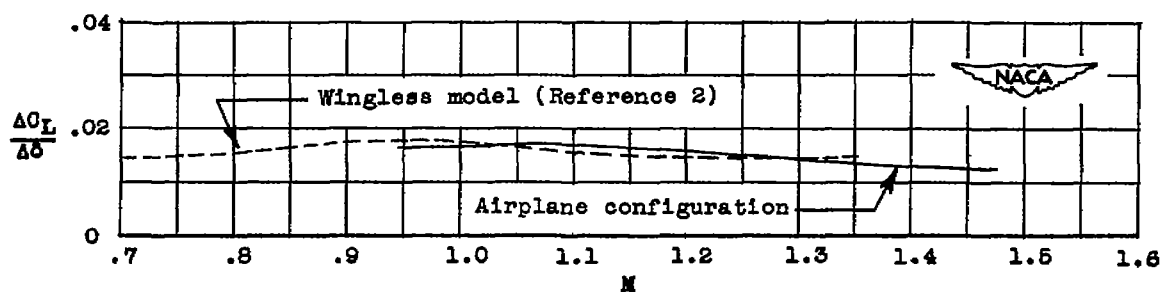
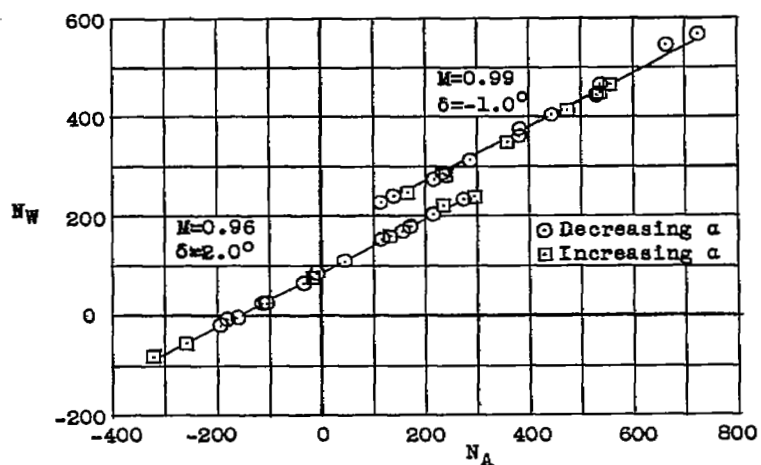
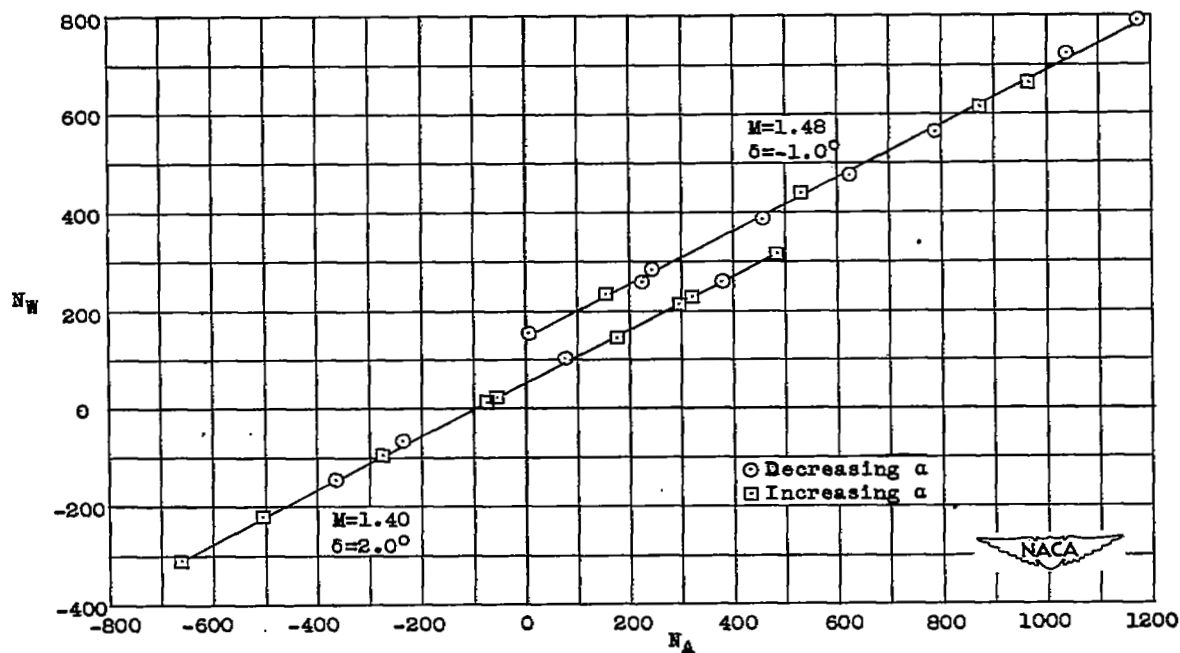


Figure 13.- Lift effectiveness of elevator.



(a) Transonic.



(b) Supersonic.

Figure 14.- Variation of wing normal force with airplane normal force during several typical oscillations.

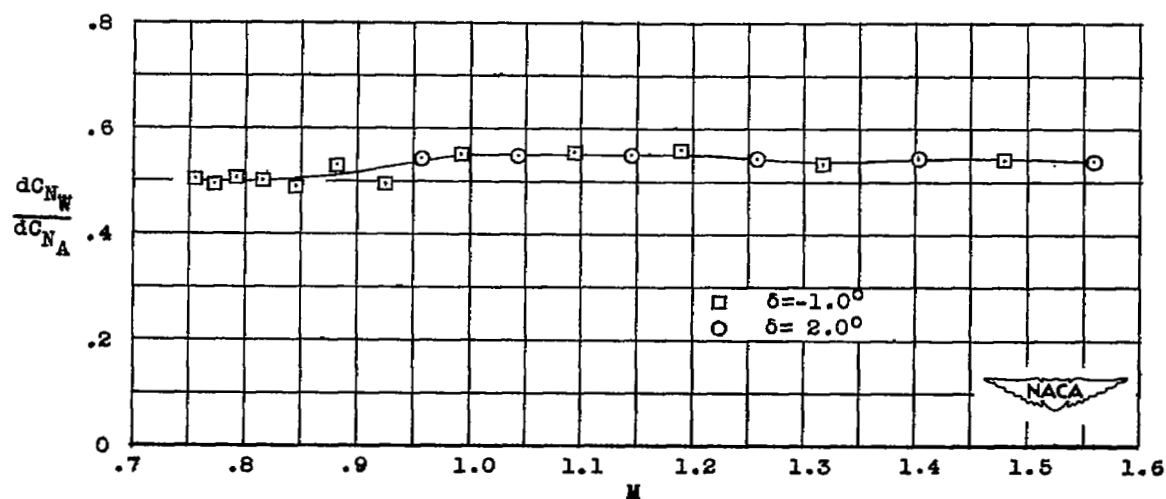


Figure 15.- Rate of change of wing normal force with airplane normal force.

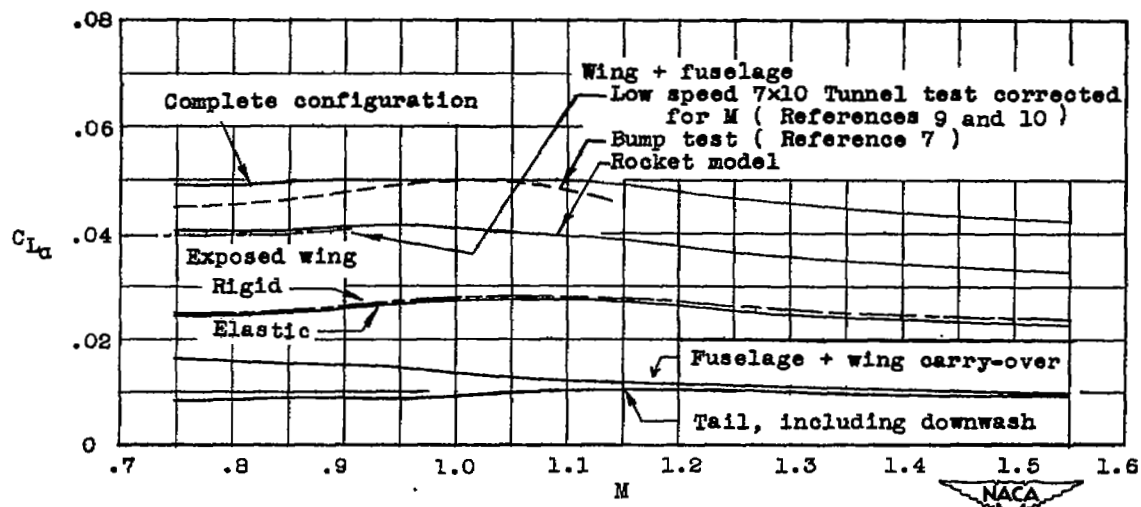


Figure 16.- Lift-curve slopes of model components.

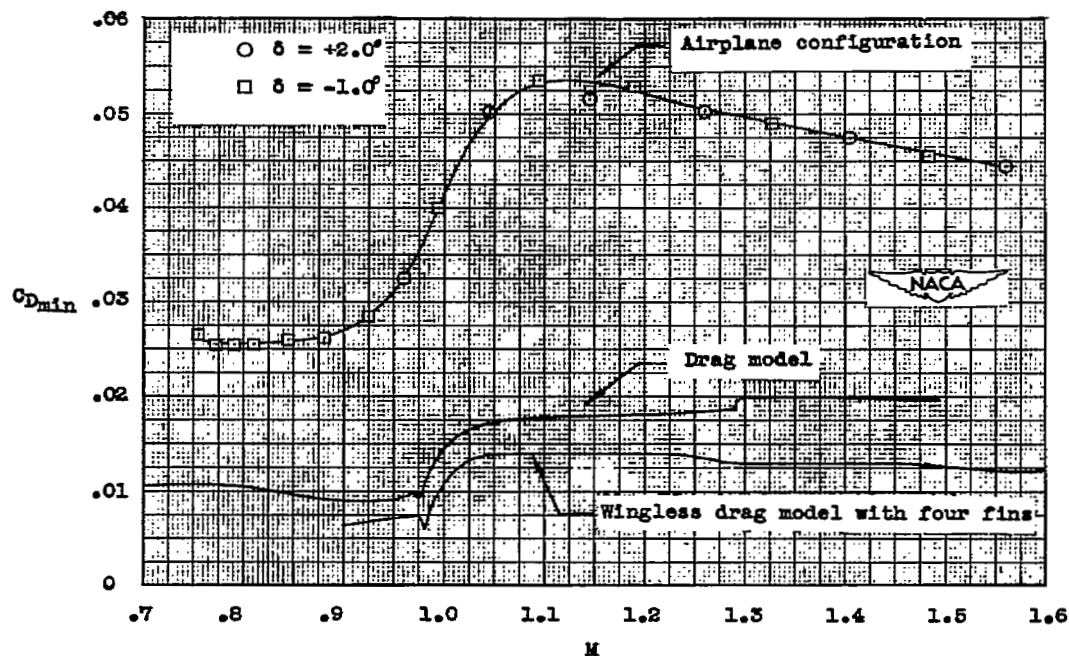


Figure 17.- Minimum drag coefficients.

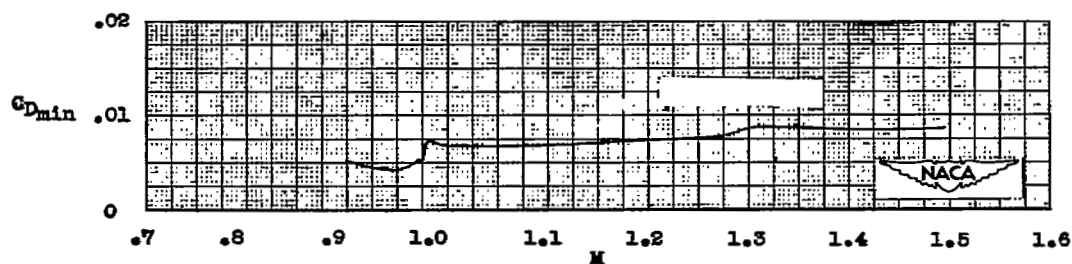


Figure 18.- Wing-plus-interference minimum drag coefficients from drag models.

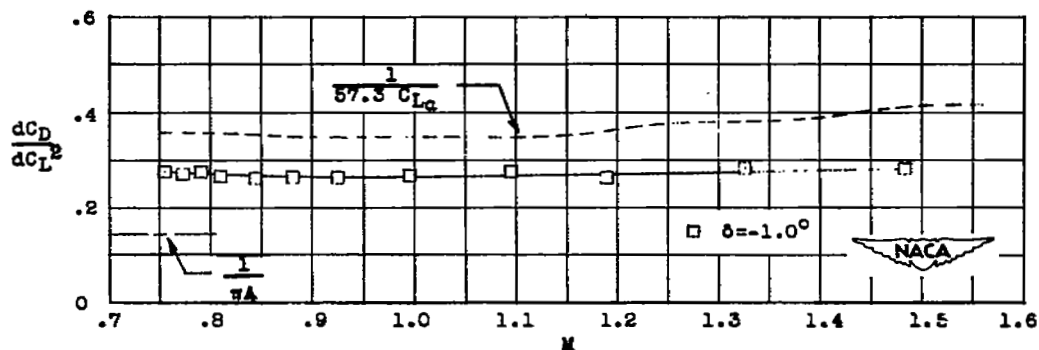


Figure 19.- Effect of lift on drag.

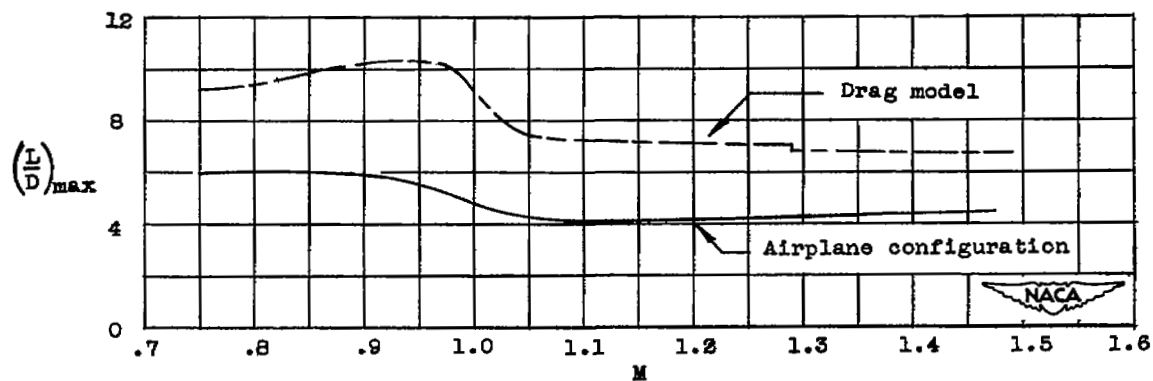


Figure 20.- Maximum lift-drag ratios.

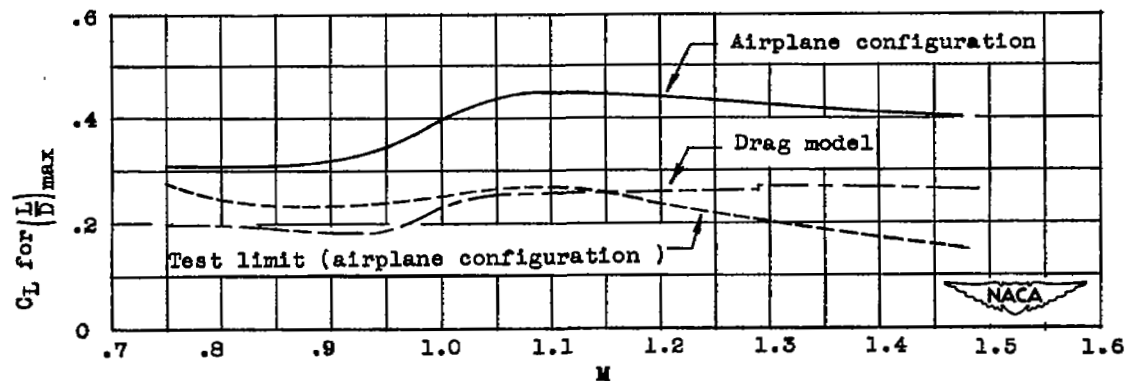
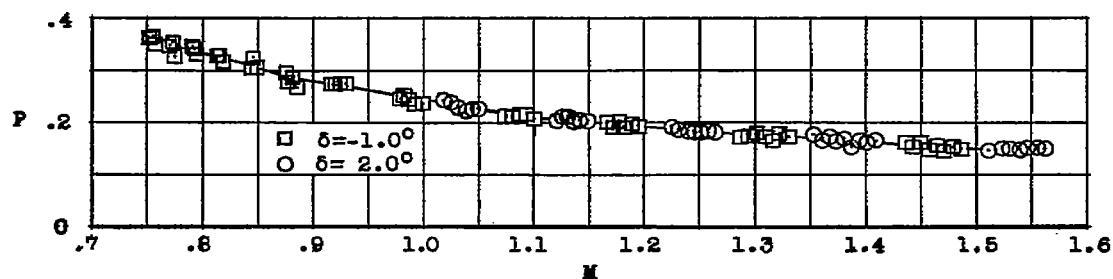
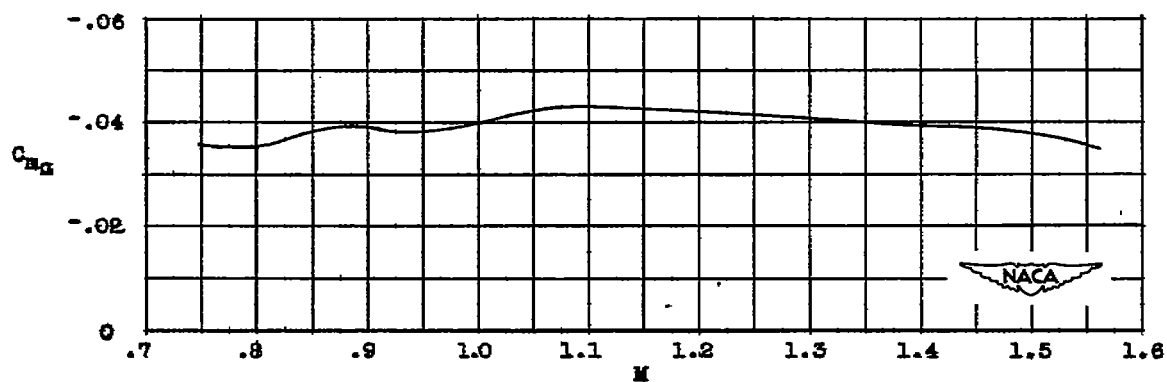


Figure 21.- Lift coefficients at which maximum lift-drag ratios occur.

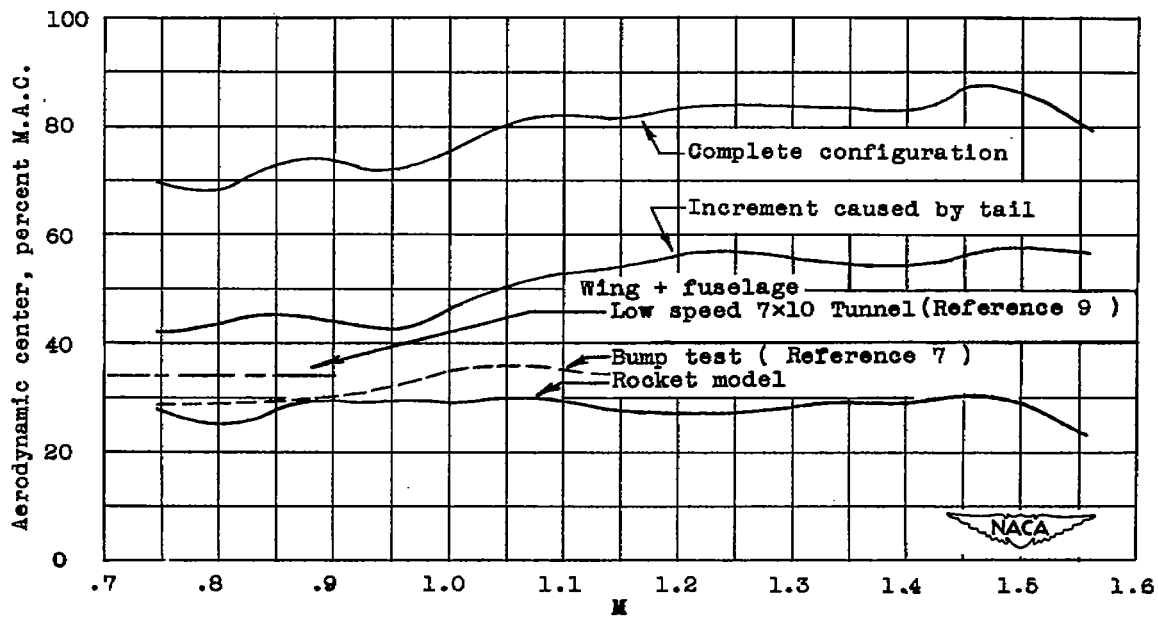


(a) Period of oscillations.



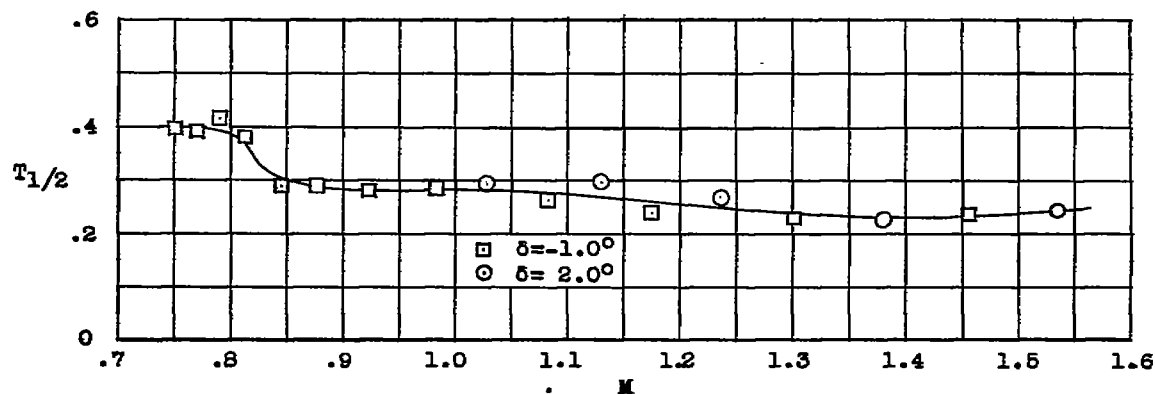
(b) Slopes of the pitching-moment curve.

Figure 22.- Static stability of model.

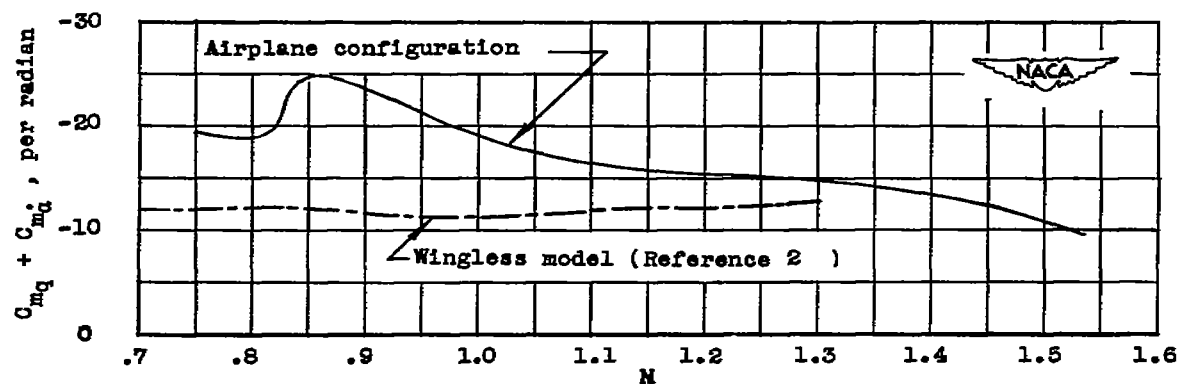


(c) Aerodynamic center of the complete model and wing-fuselage combination.

Figure 22.- Concluded.

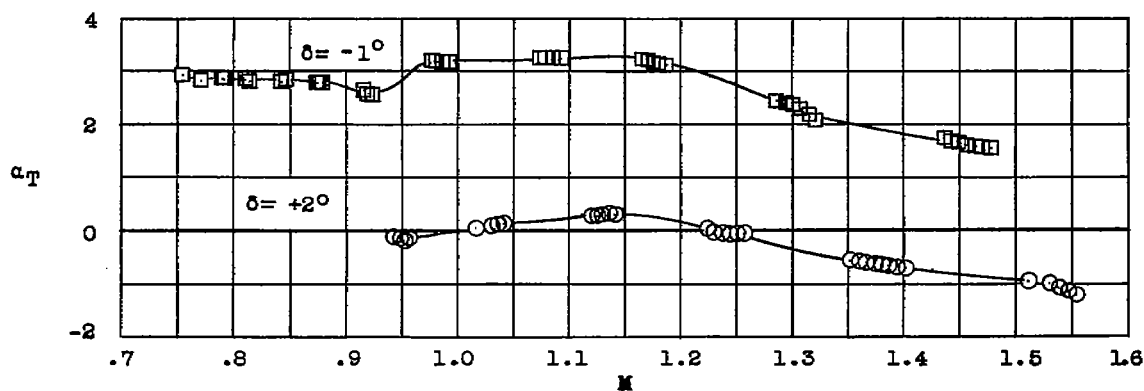


(a) Time to damp to one-half amplitude.

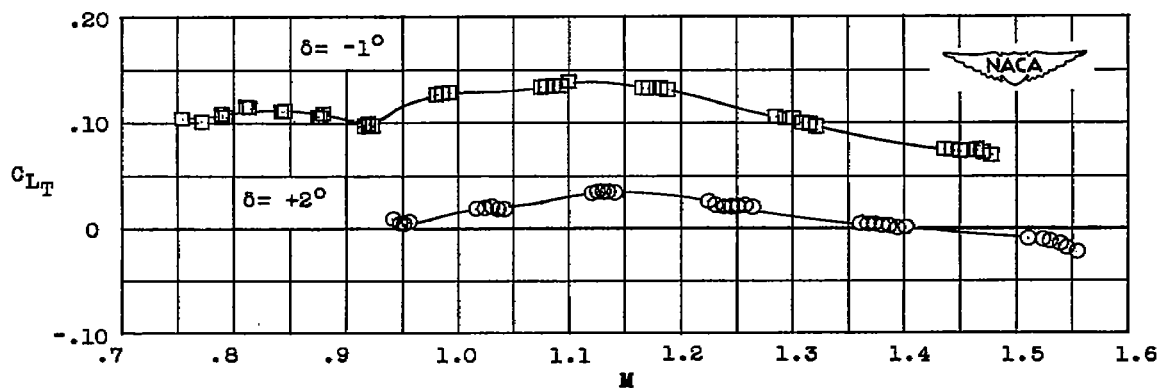


(b) Pitching-moment damping factor ($C_{mq} + C_{m_u}$).

Figure 23.- Damping characteristics of short-period oscillations.



(a) Trim angles of attack.



(b) Trim lift coefficients.

Figure 24.- Longitudinal trim characteristics.

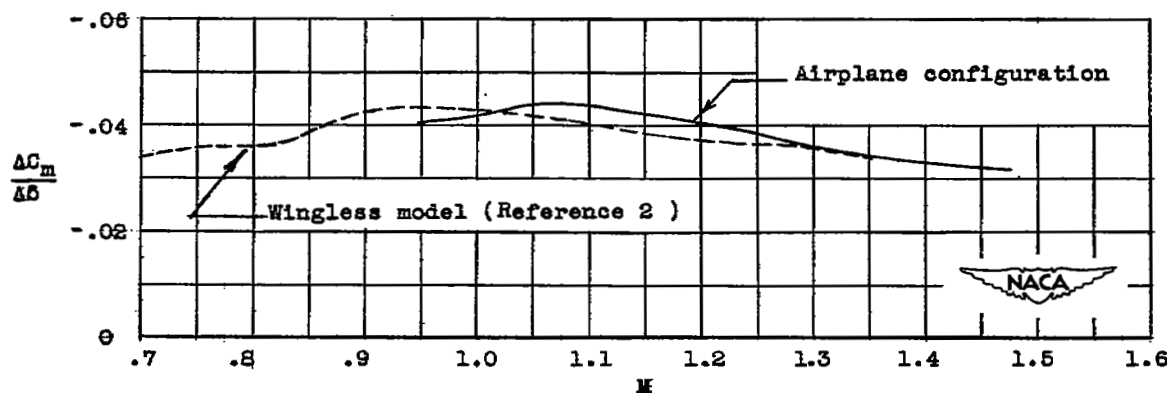


Figure 25.- Effectiveness of the elevator in producing pitching moment.

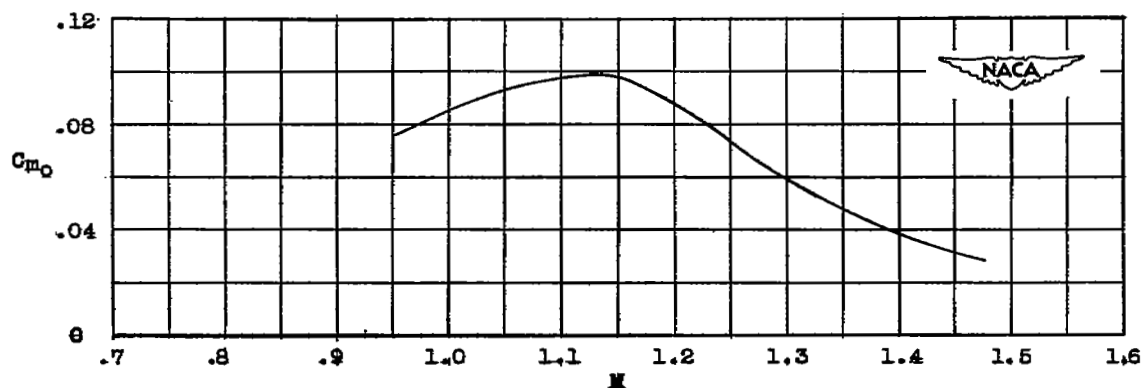


Figure 26.- Pitching-moment coefficient at zero angle of attack and zero elevator deflection.

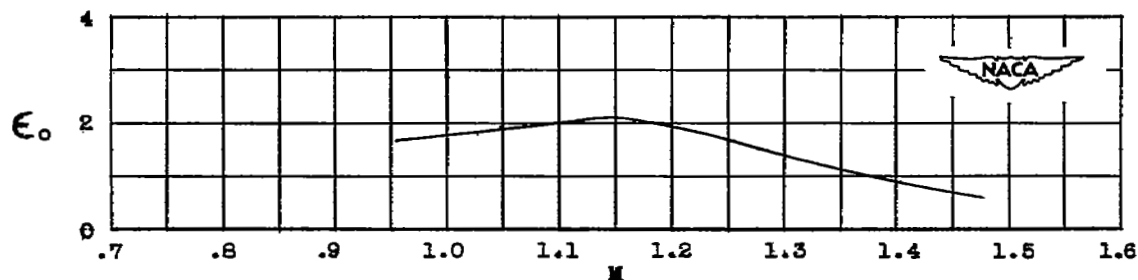


Figure 27.- Downwash angle at zero angle of attack.

SECURITY INFORMATION

NASA Technical Library



3 1176 01436 8972

~~209~~
~~5/1/56~~

